Research Square

Preprints are preliminary reports that have not undergone peer review.
They should not be considered conclusive, used to inform clinical practice,
or referenced by the media as validated information.

Revealing the hydrogeochemical characteristics and water quality of thermal springs in the Eastern Himalayan Syntaxis, Tibetan Plateau based on self-organizing map and hydrochemistry

Bingyu Yao
China University of Geosciences, Beijing
Xiaocheng Zhou
zhouxiaocheng188@163.com

China University of Geosciences, Beijing
Miao He
Institute of Earthquake Forecasting, China Earthquake Administration
Zhaojun Zeng
Institute of Earthquake Forecasting, China Earthquake Administration
Yuwen Wang
Institute of Earthquake Forecasting, China Earthquake Administration
Jiao Tian
Institute of Earthquake Forecasting, China Earthquake Administration
Ruibing Li
Institute of Earthquake Forecasting, China Earthquake Administration
Han Yan
Institute of Earthquake Forecasting, China Earthquake Administration
Yuxin Ren
Institute of Earthquake Forecasting, China Earthquake Administration
Yinglin Han
Institute of Earthquake Forecasting, China Earthquake Administration
Doudou Zha
Institute of Earthquake Forecasting, China Earthquake Administration

---

Research Article

Keywords: Eastern Himalayan Syntaxis, Thermal springs, Hydrochemistry, Source analysis, self-organizing map

Posted Date: October 26th, 2026

DOI: https://doi.org/10.21203/rs.3.rs-11318385/v1

License: This work is licensed under a Creative Commons Attribution 4.0 International License.
Read Full License

Additional Declarations: No competing interests reported.

Revealing the hydrogeochemical characteristics and water quality of thermal springs in the Eastern Himalayan Syntaxis, Tibetan Plateau based on self-organizing map and hydrochemistry

Bingyu Yao[1,2], Xiaocheng Zhou[1,2*], Miao He[2*], Zhaojun Zeng[2], Yuwen Wang[2], Jiao Tian[2], Ruibing Li[2], Han Yan[2], Yuxin Ren[2], Yinglin Han[2], Doudou Zha[2]

1.School of Earth Sciences and Resources, China University of Geosciences, Beijing 100083, China

2.United Laboratory of High-Pressure Physics and Earthquake Science, Institute of Earthquake Forecasting, China Earthquake Administration, Beijing 100036

Abstract: As a renewable energy carrier with low carbon emissions, geothermal water is globally recognized for its substantial value. This study focuses on 89 thermal springs in the Eastern Himalayan Syntaxis (EHS) on the southeastern Tibetan Plateau. By integrating self-organizing maps (SOM) with classical geochemical methods, we aim to elucidate the hydrogeochemical characteristics, genetic mechanisms, and water quality of the thermal waters in this region. The geothermal waters are classified into three groups based on SOM analysis: Group 1 (Cl-Na and HCO_3-Na), Group 2 (HCO_3-Ca and SO_4-Ca), and Group 3 (HCO_3-Ca and HCO_3-Na). The chemical composition of the geothermal waters is primarily controlled by water-rock interactions and deep fluid input, with the contributions of silicate weathering, carbonate dissolution, sulfate dissolution, and deep fluid input estimated at 33.9%, 27%, 21.1%, and 18.1%, respectively. The marked enrichment of As, B, and Li in Group 1 is attributed to reservoir rock leaching and deep fluid input. While the enrichment of F is jointly influenced by high-temperature-driven leaching of F-bearing rocks and the mechanism of fluorite dissolution-calcite precipitation. The $\delta^{18}O$ and δD value indicate that meteoric precipitation as the dominant recharge source, and the estimated reservoir temperatures for the three groups range from 142 to 277°C, 156 to 233°C, and 125 to 269°C, respectively. The entropy-weighted water quality index (EWQI) reveals that the overall water quality of the geothermal waters in the study area is poor, with As concentration being a significant controlling factor. These findings offer novel perspectives on geothermal water evolution within the EHS and provide a scientific basis for sustainable resource development and management in the area.

Key words: Eastern Himalayan Syntaxis; Thermal springs; Hydrochemistry; Source analysis; self-organizing map

1. Introduction

Within the strategic context of global energy transition and achieving the carbon peak and neutrality goals, geothermal water resources, as a clean, low-carbon, abundant, and stable renewable energy source, play a crucial role in ecological environmental protection and regional economic development (Goswami and Rai 2025; Naseer 2026). They not only have considerable potential in district heating and power generation, but also show broad application prospects in industrial and agricultural utilization, tourism, wellness, etc. (Mjami et al. 2025). Numerous countries, such as Italy, Iceland, the United States, and China, currently assign great significance to this resource and have made notable strides in its exploitation (Battistel et al. 2016; McCleskey et al. 2019; Wostbrock et al. 2018; Yuan et al. 2025). Therefore, accurately assessing the characteristics and evolution of hydrothermal systems, including the hydrogeochemistry and quality evaluation of thermal spring, is essential to resource management and utilization.

The generation and progression of geothermal water are coupled by multiple complex factors, including regional geological structures, hydrological circulation pathways, and rock-water interactions (Burnside et al. 2019; Jiménez et al. 2026). In this context, the attributes of reservoir rocks and fluid conduits are particularly critical, as they largely dictate both the origins of dissolved chemical species and the directions of subsequent geochemical evolution (Yang et al. 2024). In high-temperature geothermal systems, thermal radiation from shallow magma chambers or conductive heat flow from the deep crust can significantly intensify water-rock reactions and trigger the release of deep volatile components, further complicating the hydrochemical evolution process (Guo et al. 2019; Robidoux et al. 2025). Some laboratory experiments have also revealed that pH, temperature, and pressure notably affect the intensity of rock-water interactions, thereby altering the concentration levels of components in geothermal water. Notably, trace elements with potential hazards to human health and the environment (e.g., arsenic, fluoride) tend to become highly enriched in high-temperature geothermal systems (Morales-Simfors and Bundschuh 2022).

Assessing the geochemical characteristics of thermal springs represents a crucial initial phase for comprehending the origins and development patterns of geothermal systems. Researchers frequently rely on δD and $\delta^{18}O$ to determine the recharge sources of thermal springs and estimate the elevation of recharge (Craig 1961; Pang et al. 2017). Strontium isotopes ($^{87}Sr/^{86}Sr$) serve as a powerful indicator for reflecting the contributions of different rock types during water-rock interactions (Schmidt et al. 2017). Reservoir temperatures can be estimated using geothermal temperature scales based on cation and SiO_2 concentrations (Fournier 1977a), and mineral dissolution and precipitation behaviors can be identified by combining traditional ion ratio analysis with mineral saturation indices (Huang et al. 2026).

Currently, multivariate statistical methods, including Principal Component Analysis (PCA) and Positive Matrix Factorization (PMF), have been extensively adopted to interpret complex hydrogeochemical data and identify sources (Zhu et al. 2025). However, traditional linear statistical methods may be limited due to the frequent presence of nonlinear relationships among geochemical parameters. In recent years, the neural network algorithm based on SOM has demonstrated significant advantages in handling nonlinear geochemical data and classifying geothermal water types when combined with K-means clustering (Rahman et al. 2022; Yuan et al. 2025). Such an approach facilitates the recognition of high-dimensional features and their projection onto two-dimensional space, providing a new and reliable approach for the geochemical interpretation of complex geothermal systems. Regarding quality assessment, the EWQI, which is based on information entropy for weight assignment, has seen widespread application in groundwater quality evaluation (Liu et al. 2024b).

The Tibetan Plateau is situated within the Mediterranean-Himalayan geothermal belt, where abundant geothermal resources are exposed. Ongoing convergence between the Indian and Eurasian plates has generated a highly intricate geothermal framework in this area, giving rise to widespread and vigorous hydrothermal activity. Currently, hundreds of medium-high temperature hydrothermal systems have been found on the southern, middle, and northern parts of the Tibetan Plateau, including representative systems such as the Yangbajing, Gulu, and Gonghe Basin geothermal systems (Lu et al. 2024; Wang et al. 2022; Zhou et al. 2023). The EHS, located at the easternmost margin of the southern Tibetan Plateau, serves as the core zone of the collision. As an important geological hub linking between the high-temperature hydrothermal systems of southern Tibet and western Sichuan, the EHS hosts numerous thermal springs along its east-west trending deep sutures and fault zones. Research has shown that geothermal waters in this region are predominantly of HCO_3-Na type, derived from a common deep parent fluid and recharged by deep magmatic fluids (Cao et al. 2025; Li et al. 2021). Conversely, geothermal waters in the Sanjiang orogenic belt, located to the northeast of the EHS, are mainly controlled by lithology and dissolution processes, with no involvement of magmatic fluids (Yi et al. 2021). Nevertheless, comprehensive investigations of geothermal waters in the EHS and its adjacent areas remain relatively limited, particularly regarding the sources, enrichment mechanisms, and environmental effects of harmful chemical components in the geothermal waters. Therefore, the present work seeks to: (1) discern distinct chemical signatures of various thermal springs clusters via SOM combined with K-means clustering; (2) examine recharge sources and water-rock interactions by integrating conventional hydrochemical assessments with multivariate statistical approaches; and (3) characterize the spatial distribution of toxic constituents and evaluate the overall quality of thermal waters. The findings of this study will enhance the understanding of the genetic evolution of the EHS geothermal systems and provide insights to support the sustainable development and

management of geothermal resources.

2. Study area

The Tibetan Plateau, as the largest and highest plateau on Earth, owes its primary formation to the collision and persistent convergence of the Indian and Eurasian plates (Tapponnier et al. 2001; Xu et al. 2016). Meanwhile, it is also one of the most geothermally active regions in the world. Throughout the evolution of the Tethys Ocean, several continental fragments progressively accreted onto the southern edge of the Asian continent, producing, from south to north, the Himalayan, Lhasa, Qiangtang, and Bayanhar terranes (Xu et al. 2006). These blocks are bounded by several major suture zones sequentially from north to south: the Jinsha Suture Zone (JSZ), the Bangong-Nujiang Suture Zone (BNSZ), and the Yarlung Tsangpo Suture Zone (YTSZ) (Xu et al. 2006). The eventual closing of the Neo-Tethys Ocean gave rise to the present-day geological framework (**Fig. 1**a). The East Himalayan Syntaxis, situated in the southeastern of the Tibetan Plateau, represents the leading edge of the ongoing Indo-Eurasian plate convergence (Ding et al. 2001; Xu et al. 2012). This region experiences exceptionally high tectonic stress, rapid rates of geomorphic evolution, and intense Cenozoic metamorphism and magmatic activity (Xu et al. 2012).

Structurally, the study area encompasses the eastern parts of the Lhasa and Qiangtang blocks, which are bounded by the BNS and JS, respectively (**Fig. 1**a). Around the EHS, strike-slip faults and a series of secondary faults are well developed, predominantly trending nearly E-W and N-S (Tang et al. 2010). These faults include the Yarlung-Tsangpo, Jiali, Nujiang, Lancangjiang, and Jinshajiang faults. Since the collision, these faults have remained active with thrust-slip characteristics. They penetrate deeply into the crust and may even extend into the asthenosphere, controlling the distribution of Cenozoic magmatic rocks and geothermal fields in the region (Li et al. 2021). Topographically, the area surrounding the EHS is characterized by high mountains with elevations exceeding 4,000m and a high mountain-gorge landscape formed by rivers such as the Yarlung Tsangpo, Nujiang, Lancang, and Jinsha rivers (Song 2010).

The EHS exhibits a complex assemblage of strata and lithologies (**Fig. 1**b). In the southern part of the Lhasa block, a typical sequence of Carboniferous, along with the Nyainqêntanglha Group gneisses, banded migmatites, and the Mesozoic Yarlung-Tsangpo ophiolitic mélange are developed (Xu et al. 2012). In contrast, the Qiangtang block is primarily composed of folded belts, with its strata comprising mainly Triassic and Jurassic sedimentary sequences and granites (Yi et al. 2021). The Triassic strata consist mainly of sandstone and carbonate rocks, whereas the Jurassic strata are chiefly composed of sandstone, shale, and rare gypsum. Magmatic activity of diverse origins and stages occurred frequently within the EHS, particularly during the Yanshanian and Himalayan periods (Liu et al. 1996). The Cretaceous-Paleogene Gangdese granite belt, associated with the subduction and closure of the Tethys

Ocean and subsequent continental collision, is extensively distributed in southern Tibet (Xu et al. 2012).

The study area belongs to southeastern Tibet, where hydrothermal activity is highly developed. According to the latest geothermal heat flow map of mainland China, the values of geothermal background in this study area range from 75 to 150 mW/m^2, demonstrating a distinct thermal anomaly (Jiang et al. 2019). Most thermal springs are distributed in bands along E-W trending active faults or densely fractured zones, manifesting as low-medium temperature thermal springs (25-60°C), while some are classified as high-temperature springs (>60°C). At present, the development and utilization of geothermal water resources in the study area are primarily based on the direct use of thermal springs, with an annual utilization volume reaching approximately 1.589×10^{6}m^3, indicating favorable prospects for further exploitation (Zhang et al. 2023).

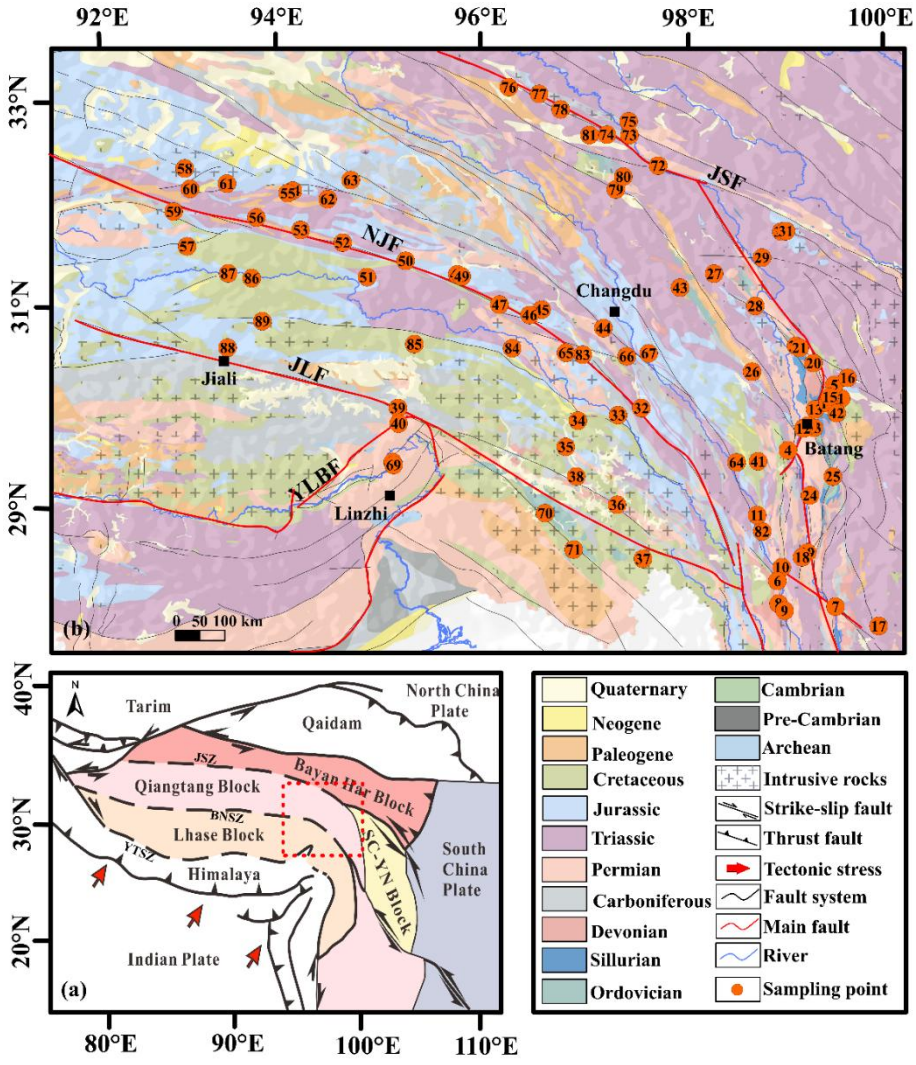


Fig. 1 (a) Tectonic architecture of Tibetan Plateau. YTSZ: Yarlung Tsangpo Suture Zone; BNSZ: Bangong-Nujiang Suture Zone; JSZ: Jinsha Suture Zone. (b) Geological map of the study area. YLBF: Yarluzangbu Fault; JLF: Jiali fault; NJF: Nujiang fault; JSJF: Jinsha fault

3. Materials and methods

3.1 Water sampling and testing

In the EHS, a total of 89 water samples were collected. Prior to laboratory analysis, each sample was passed through a 0.45 μm filter and then stored in 50 mL polyethylene terephthalate (PET) bottles. For those designated for cation and trace element determination, HNO_3 was added to reduce the pH value to below 2. Field measurements of physical parameters, specifically temperature and pH, were conducted using a portable HACH multi-parameter analyzer (model HQ40D).

Major ions were tested in the Key Laboratory of Earthquake Prediction, China Earthquake Administration using a Dionex ICS-900 (Thermo Fisher, USA) ion chromatograph, with a detection limit of 0.01 mg/L. The HCO_3^- and CO_3^{2-} were calculated by a titration procedure using the 0.05 mol/L HCl titration, with 0.1% methyl orange and 1% phenolphthalein as indicators (reproducibility within ±2%). Trace elements and strontium isotopes were analyzed using an element type inductively coupled plasma mass spectrometer (Agilent8900, USA) and hot surface ionization-mass spectrometer (Phoenix, USA) at the Test Center of the Beijing Research Institute of Nuclear Industry Geology. Arsenic quantification was carried out using an LC-6500 atomic fluorescence photometer, achieving a detection limit of 0.60 μg/L. SiO_2 was determined by an inductively coupled plasma emission spectrometer Optima-5300 DV (PerkinElmer, USA). The $\delta^{18}O$ and δD were analyzed with a Finnigan MAT253 (Thermo Electron-Finnigan, USA) spectrometer, which are standardized using V-SMOW, with analytical uncertainty of ±0.2‰ and ±1‰, respectively. All samples were tested for charge balance error (CBE) detection according to the following formula:

$$CBE(\%) = \frac{\sum cations - \sum anions}{\sum cations + \sum anions} * 100\% \quad (1)$$

The CBE of all samples in the study were within ±5%.

3.2 Self-Organizing Map

Introduced by Kohonen in the 1980s, the SOM represents an unsupervised neural network that aims to reduce dimensionality and visualize data (Kohonen 1982). It accomplishes this by projecting high-dimensional input onto a lower-dimensional node grid, typically two-dimensional. Additionally, Because the SOM algorithm alone lacks the ability to automatically ascertain the optimal number of clusters, its output can subsequently serve as input for the K-means algorithm, which more effectively recognizes and interprets underlying patterns and relationships within the dataset. For detailed explanations of the SOM and K-means clustering procedures, including calculation steps, is provided in text S1. This study used the Heuristic rules to select the map size, i.e., $5\sqrt{n}$ (n being the number of samples), taking into account the minimum values of both quantitative error (QE=1.28) and terrain error (TE=0.03). Ultimately, an 8×6 architecture was selected as the optimal output neuron with 1000 training iterations, generating each component

plane. The data were normalized prior to analysis.

3.3 Positive matrix factorization (PMF) model

For quantitative source identification of hydrochemical constituents, the PMF model was adopted in this work. Following protocols established by the U.S. Environmental Protection Agency (EPA), the EPA PMF 5.0 software decomposed the measured concentration data into several probable contributing sources and determined each source's relative contribution rate. A full description of the operational steps appears in text S2. This study included eight indicators (Na, K, Mg, Ca, Cl, SO_4^{2-}, HCO_3^-, TDS) in the PMF model. Uncertainties were calculated using Equations S5 and S6, with the error fraction set to 0.15. The signal-to-noise ratio (S/N) for various parameters ranged from 5.7 to 9.0. Exploratory PMF analyses were conducted for 2 to 6 factors, with 20 iterations performed. The model performance was optimized at 4 factors, at which point Q_{true} and Q_{robust} were closest (Q_{true}/Q_{robust} = 1.08), and all standard residuals fell within the range of −3 to 3. Except for Mg^{2+} (R^2 = 0.32), the R^2 values of the remaining parameters were close to 1, indicating that the model results have good applicability.

3.4 Entropy-weighted water quality index

To evaluate the quality of springs, this research applied the EWQI. This index reduces the subjectivity associated with conventional weight assignment methods, leading to more objective results (Abidi et al. 2024). The detailed calculation steps can be found in text S3. In this study, according to the rank III threshold in Standard for groundwater quality of China (GB/T 14848-2017), water quality can be divided into five categories as per the results of EWQI: Rank I, Excellent (EWQI <50); Rank II, good (50 < EWQI <100); Rank III, medium (100 < EWQI <150); Ranke IV, poor (150 < EWQI <200); Rank V, very poor (EWQI >200) (Mia et al. 2023).

3.5 Geochemical calculation

The saturation index (SI) of minerals offers a qualitative means of discerning which phases are prone to precipitation or dissolution during water-rock interactions. The PHREEQC software 2.12.5 is used to calculate the SI based on the Eq.2

$$SI = \log(\frac{IAP}{Ks}) \quad (2)$$

where *IAP* is the ionic activity product of mineral components, and *Ks* is the solubility product constant of a mineral. SI > 0 indicates supersaturation; SI < 0 indicates unsaturation.

To estimate the reservoir temperatures of geothermal water, we employ calculations using quartz and chalcedony geothermometers (Fournier 1977b; Giggenbach et al. 1983). Additionally, the silicon enthalpy equation was used to calculate the reservoir temperature prior to mixing with cold water.

$$\text{Quartz (Maximum steam loss): } T = [1522 / (5.75 - \lg(SiO_2))] - 273.15 \quad (3)$$

$$\text{Quartz (no stream loss): } T = [1309 / (5.19 - \lg(SiO_2))] - 273.15 \quad (4)$$

$$\text{Chalcedony: } T = [1032 / (4.69 - \lg(SiO_2))] - 273.15 \quad (5)$$

$$H_cX + H_h(1 - X) = H_s \quad (6)$$

$$Si_cX + Si_h(1 - X) = Si_s \quad (7)$$

where H_c is the enthalpy of cold water (cal/g); H_h is the enthalpy of the geothermal water (cal/g); Hs is the enthalpy of the thermal spring (cal/g); Sic is the concentration of SiO_2 in the cold water (mg/L); Si_h is the concentration of SiO_2 of the geothermal water (mg/L); Sis is the concentration of SiO_2 in the thermal spring (mg/L). In this study, Hc and Sic values are obtained from the average values of the cold spring temperature and SiO_2 in the samples (Hc= 16.14 cal/g, SiO_2 = 12.36 mg/L). The enthalpy and SiO_2 content of deep geothermal waters are obtained from reference (Fournier and Truesdell 1974).

Using the Eq.8, the circulation depth of thermal springs is estimated from reservoir temperatures.

$$D = d + \frac{T_R - T_C}{\Delta t} \quad (8)$$

where D is the circulation depth (m); d represents the constant temperature zone (m), with an average value of 20m; T_R represents the reservoir temperature (°C); T_C represents the local annual average temperature (5℃); Δt represents the local geothermal gradient (36°C/km) (Liao et al. 2020).

4. Results

4.1 Hydrochemical composition of thermal spring

Table S1 presents the results of component measured for the water samples. The discharge temperatures range from 8.0 ℃ to 89.0 ℃. According to water sanitary requirements and management specification of hot spring tourism in China (LB/T 081-2020), 82% of the samples (n=73) can be considered as hot springs (T>25 ℃), while the remaining 18% of the samples (n=16) are cold springs (T<25 ℃). The pH values range from 6.40 to 9.41, namely acidic to weakly alkaline. Total dissolved solid (TDS) values of samples widely range from 230.4 to 4019.8 mg/L. For the most samples, Na^+ and HCO_3^- are the most abundant cations and anions, with concentrations ranging from 4.88-954.94 mg/L and 111.04-1739.45 mg/L, respectively. While the concentrations of Br^-, NO_3^-, and CO_3^{2-} are low, with the mean values of 0.47 mg/L, 1.43 mg/L, and 40.18 mg/L, respectively. The concentrations of F^- range from 0.1 to 20.7 mg/L, with the mean of 4.1 mg/L.

The test results of trace elements were shown in Table S2. The concentrations of dissolved elements of water samples vary a lot. For the typical trace element (As, B, Li) in the geothermal system, the concentrations range from <0.60 to 1905 μg/L, 20.3 to 33464 μg/L, and 3.2 to 14667 μg/L, respectively. While some dissolved heavy metal elements, such as Fe and Mn, with concentrations range from 0.4-9491 μg/L and 0.06-1973 μg/L.

4.2 SOM–KM clustering results

For the purpose of better illustrating distinctions among the 89 water samples, this study

uses the SOM for classification, yielding corresponding output neurons. Each physicochemical parameter is displayed as a map, where red representing high values and blue representing low values. By examining the color gradients across these planes, potential correlations among variables can be visually presented. The SOM visualization results show that Na^+, K^+, and Cl^- exhibit similar distribution patterns (**Fig. 2**), all displaying higher color gradient values in the lower left corner, indicating they may undergo similar hydrochemical processes. Additionally, Ca^{2+} and SO_4^{2-} show a strong correlation, suggesting they may have a common source. The high-value areas of Mg^{2+} are concentrated in the upper right corner, and higher concentrations mostly appear in cold spring samples.

Based on the SOM analysis results, we subsequently apply K-means clustering to partition the thermal waters into three distinct groups (**Fig. 2**). Group 1 is characterized by relatively high concentrations of Na^+ (197.80-954.94mg/L), K^+ (10.17-101.48mg/L), Cl^- (9.09-1151.12mg/L), and HCO_3^- (510.71-1739.45mg/L), with hydrochemical type dominated by Na-HCO_3 and Cl-Na (**Fig. 3**). This group also exhibits higher contents of As, B, and Li (**Fig. 4**), with average concentrations of 450.2μg/L, 9669.2μg/L, and 2912.2μg/L, respectively. Group 2 features relatively high concentrations of Mg^{2+} (16.7-208.9mg/L), Ca^{2+} (20.9-650.2mg/L), SO_4^{2-} (22.57-1969.25mg/L), and total TDS (626.8-4019.8mg/L), with hydrochemical types mainly classified as HCO_3-Ca and SO_4-Ca (Mg) (**Fig. 3, 4**). Group 3 shows relatively high F^- concentrations and pH values, with a broader distribution of hydrochemical types, including Na-HCO_3 and Ca-HCO_3 (**Fig. 3, 4**).

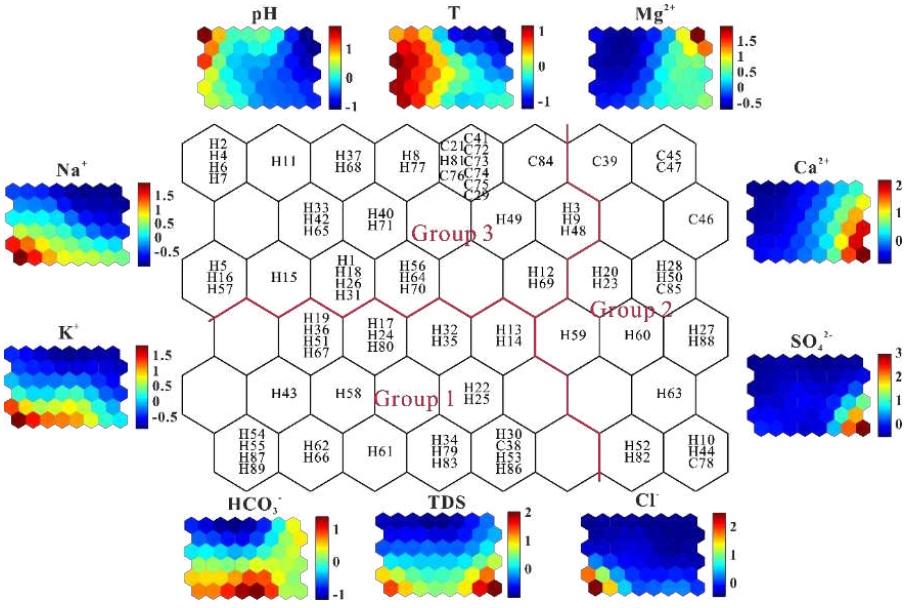


Fig. 2. Component planes and clustering result in the SOM analysis.

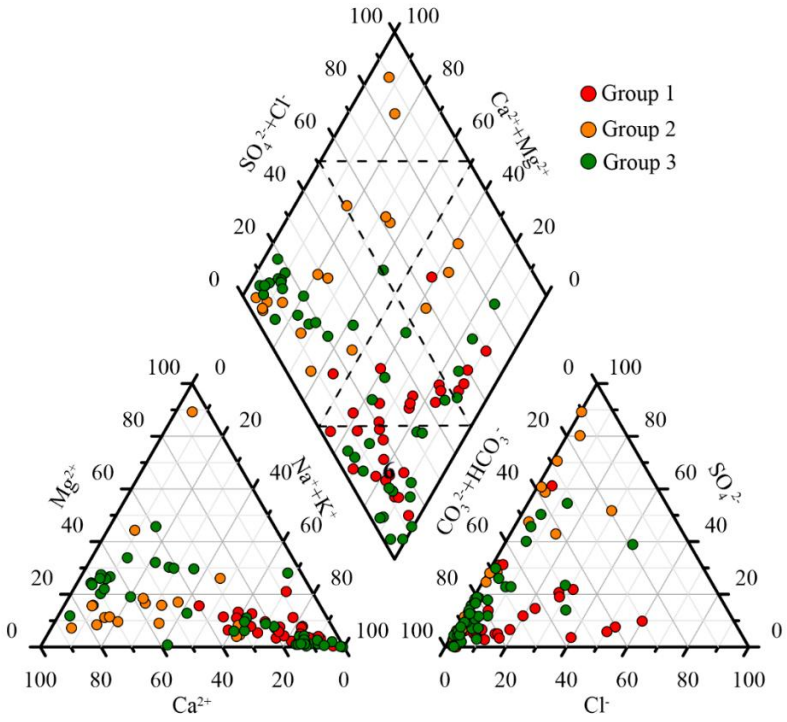


Fig. 3. Piper diagram for the water samples in the EHS.

4.3 δD, $\delta^{18}O$ and $^{87}Sr/^{86}Sr$ isotope characteristics

The isotopic compositions are listed in Table S1. The δD, $\delta^{18}O$, and $^{87}Sr/^{86}Sr$ values of Group 1 range from −158.7‰ to −100.7‰, −20.8‰ to −12.3‰, and 0.713899 to 0.733246, respectively. The δD, $\delta^{18}O$, and $^{87}Sr/^{86}Sr$ values of Group2 are in the range from −144.7‰ to −92.0‰, −18.8‰ to −12.0‰, and 0.707772 to 0.720637, respectively. The δD, $\delta^{18}O$, and $^{87}Sr/^{86}Sr$ values of Group 3 range from −161.6‰ to −77.5‰, −21.2‰ to −10.9‰, and 0.708226 to 0.739091, respectively.

4.4 Water quality assessment of springs

Although due to the high temperature and high TDS content of geothermal springs, it is rarely directly used as drinking water, most of these thermal springs in the EHS will naturally discharge and flow into surface rivers or replenish shallow groundwater systems, posing environmental risks. So this study uses EWQI method to comprehensively evaluate the water quality of springs in the EHS based on 14 chemical parameters. The entropy weighting approach yielded the relative weight of each parameter for the comprehensive water quality assessment. The results indicate that Zn and As are the most influential factors, with weights of 0.23 and 0.13 (Table S3), respectively, suggesting that these two elements are the key indicators controlling the water quality. The statistical summary of the EWQI values is presented in the Table S3 and (**Fig. 5**a). The values of EWQI vary widely, ranging from 3.4 to 4123.3. Among the samples, 58.4% are classified as having water quality ranging from Excellent to Medium,while the remaining 41.6% fall into lower categories. Based on grouping statistics, Group 1 exhibits the poorest water quality, followed by Group 2, while Group 3 shows

relatively better water quality. Notably, the spring with poor water quality in the EHS are mostly located near the NJF (**Fig. 5**b), and the spatial variation of EWQI shows similarities with the spatial distribution patterns of As, B, and Li (Fig. S1), indicating that areas with higher concentrations of typical deep-sourced elements in geothermal system tend to have poorer water quality.

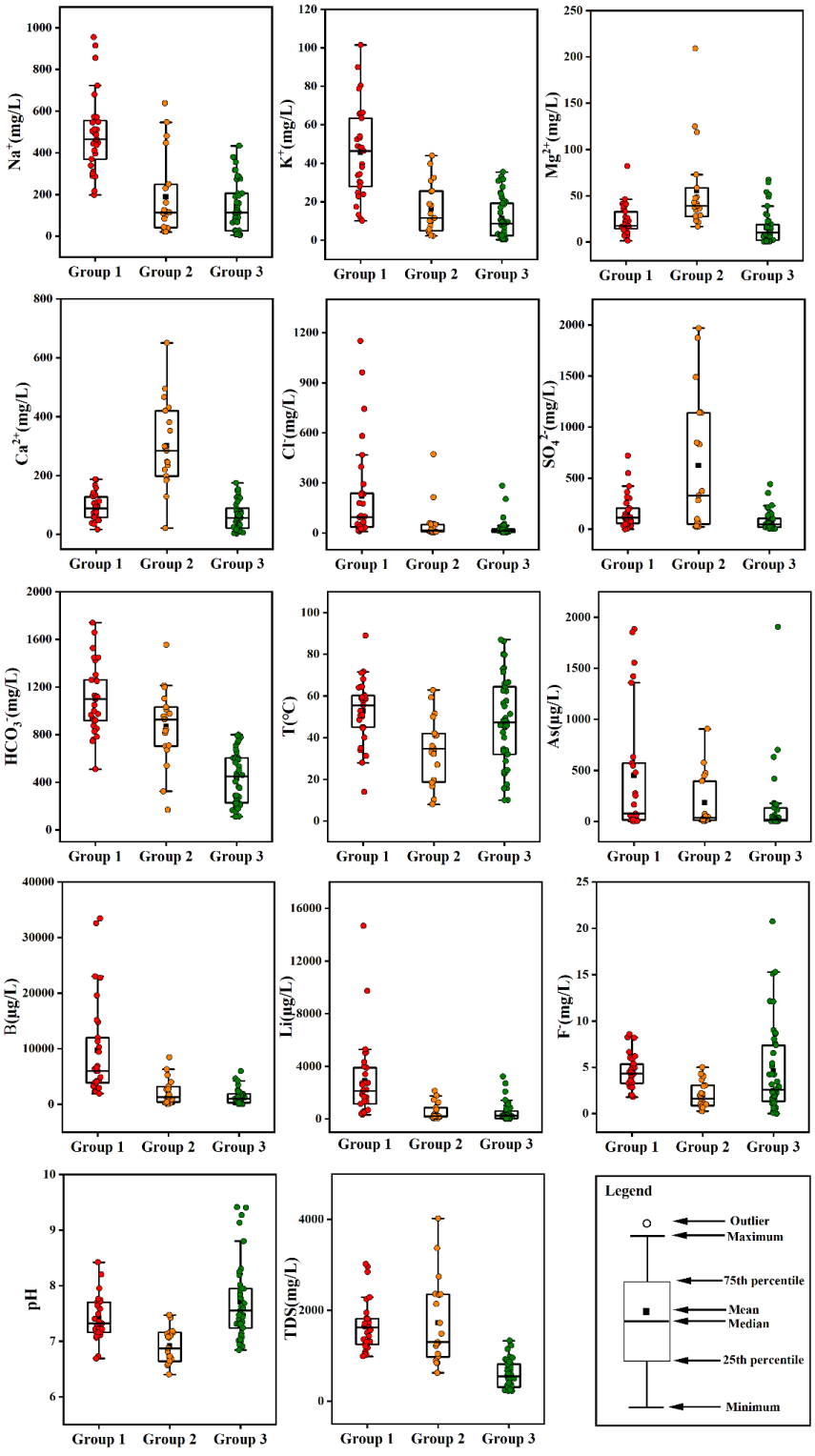


Fig. 4. Statistical charts depicting the hydrochemical parameters of water samples in the three groups.

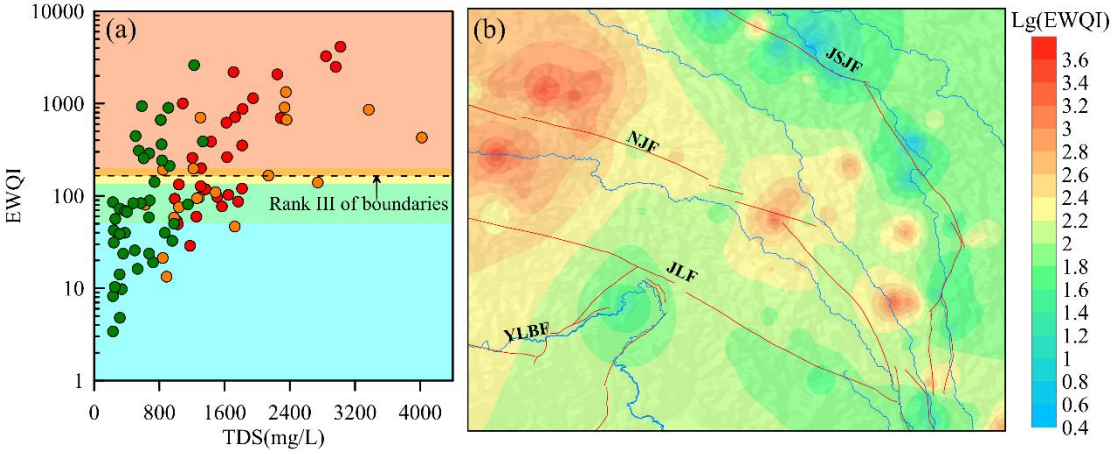


Fig. 5. (a) Scatter plot of EWQI and TDS, (b) the spatial distribution map of EWQI.

5. Discussion

5.1 major factors influencing hydrochemistry

To explore the sources of ions in different types of springs and the main factors controlling hydrochemistry, this study combined principal component analysis (PCA) and PMF to quantitatively analyze the chemical ion sources of thermal springs. Three components were extracted through PCA, accounting for 78.32% of the total variance (**Fig. 6)**, and four main controlling factors were identified based on the PMF model (**Fig. 7)**.

PC1 explained 38.81% of the total variance, with Na^+, K^+, Cl^-, TDS, and HCO_3^- exhibiting high positive loading, and these parameters were highly correlated with each other (**Fig. 6**a). The PMF decomposes PC1 into F3 and F4, with their respective contribution rates being 18.1% and 33.9%. In the F4, the contributions of Na^+ (68.9%), K^+ (78.4%), HCO_3^- (59.4%), and TDS (39.8%) were particularly significant. Na^+ and K^+ in geothermal water typically originate from the dissolution of silicate minerals or halite, and cation exchange. In the **Fig. 8**a, nearly all samples below the 1:1 line, suggesting that the dissolution of halite is not the principal source of Na^+ and Cl^- (Li et al. 2025). While the excess Na^+ and K^+ may originate from the dissolution of silicate minerals or cation exchange reactions (Eq. 9, 10, 11). In the **Fig. 8c**, all samples are scattered near the line y = -x, indicating the occurrence of cation exchange. The chloro-alkaline indices (CAI–I and CAI–II) confirmed Ca^{2+} in the geothermal waters was replaced by Na^+ in the reservoir rock (Fig. S2). The HCO_3^- can be contributed by the dissolution of silicates and carbonates. In the **Fig. 8**g, h, some of samples in the Group 3 and 2 fall on the calcite and dolomite dissolution lines dissolution line (Eq. 14, 15). This suggests that the dissolution of Triassic carbonate rocks plays a significant role in such groups. In comparison, the samples in the Group 1 significantly above the mineral dissolution lines, exhibiting excess HCO_3^-. Previous studies have found that the $\delta^{13}C$ values of CO_2 in geothermal gases from the EHS range from −3.54‰ to −3.91‰, indicating that the CO_2 source is constrained by both the decarbonation of carbonate rocks and mantle-derived volatile (Li et al. 2024). Therefore, the excess HCO_3^- observed in Groups 1 and 3 likely originates from the dissolution of silicate

minerals facilitated by CO_2-rich fluids (Eq. 9, 10). In addition, the ratio of (Ca + Mg)/(HCO_3+SO_4) serves as an indicator of the proportional influence exerted by silicate and carbonate dissolution to hydrochemical composition (Yuan et al. 2025). In this study, some samples from Groups 3 and 2 near the 1:1 line, indicating that their hydrochemical composition is primarily controlled by carbonate dissolution (**Fig. 8**b). In contrast, most samples above the 1:1 line, suggesting that the dissolution silicate mineral is the dominant process governing hydrochemical evolution. Based on the above analysis, F4 can be interpreted as representing the primary water-rock interaction processes that control hydrochemistry, including the dissolution of silicate minerals and cation exchange.

The Cl^- contributed the most to F3 (83.2%). In geothermal systems, Cl^- is generally considered to originate from the leaching of halite-bearing strata, seawater mixing, or contributions from deep fluids (Guo 2012; Pan et al. 2021; Robidoux et al. 2025). In this study, Cl^- concentrations vary considerably among the three groups (**Fig. 4**). Specifically, some water samples in Group 1 (e.g., H54, H55, H62, H66, H87, and H89) show anomalously high Cl^- concentrations (>500 ppm), whereas Groups 2 and 3 generally display low Cl^- levels. Calculations of the saturation indices (SI) for halite indicate that all samples are undersaturated (Fig. S3). Taking into account the widespread occurrence of metamorphic rocks (such as gneiss) and granite intrusions in the EHS, the elevated Cl^- concentrations are unlikely to result from halite dissolution. Furthermore, as the study area is located inland, seawater mixing can also be largely excluded. Similar high Cl^- concentrations have been widely reported in geothermal systems on the Tibetan Plateau and elsewhere. For instance, Cl^- concentrations exceed 1000 ppm in the Yangbajing geothermal water in southern Tibet (Luo et al. 2025), range from 300 to 900 ppm in some geothermal waters from the Gonghe Basin in northeastern Tibet (Lu et al. 2024), and reach up to 720 mg/L in the Kiejo-Mbaka geothermal springs within the East African Rift System (Kobare et al. 2025). Such anomalously high Cl^- concentrations are typically attributed to mixing with magmatic-derived fluids, indicating a significant contribution of deep geothermal fluids (Pan et al. 2021). In the EHS, helium isotopic data from the hydrothermal system reveal that the contribution of mantle-derived helium can reach up to 7.52%, suggesting the involvement of deep fluids in the formation of the geothermal waters (Li et al. 2024). The samples with higher Cl concentrations in Group 1 have higher $^3He/^4He$ ratios (Fig. S4). Thus, F3 can be interpreted as the contributions from the mixing of deep fluids. Notably, the higher scores (median = 0.83) for PC1 in Group 1(**Fig. 6**b**)** indicate that the leaching of silicate minerals involving deep fluids is the primary factor controlling the hydrochemical composition of this group. Its hydrochemical types are Na-HCO_3 and Na-Cl, exhibiting characteristics similar to those of typical deep-circulating high-temperature geothermal water. This geochemical signature is consistent with findings previously reported for geothermal waters in the Cuona-Woka Rift and Kangding on the Tibetan Plateau (Li et al. 2018b; Yuan et al. 2025).

PC2 explained 27%, characterized by a high positive loading of Mg^{2+} and a moderate positive

loading of HCO_3^-, while T and pH showed negative loading. Meanwhile, F1 (27% contribution) also includes Mg^{2+} (79.4%), Ca^{2+} (60.1%), and HCO_3^- (38.4%). This feature reflects the dissolution process of carbonate minerals under low-temperature conditions and is closely related to the Triassic carbonate rocks that are widely distributed in the shallow subsurface of the EHS. As mentioned above, the dissolution of carbonate minerals determined the hydrochemical composition of some samples in the Group 2 and Group 3. PC3 explained 12.51%, with high positive loading of Ca^{2+} and SO_4^{2-}.This feature corresponds to F2, in which $SO_4^{2-}$and Ca^{2+} account for 91.2% and 33.8%, respectively, reflecting the water-rock reaction process related to SO_4^{2-}. In the relationship diagram between Ca^{2+} and SO_4^{2-} (**Fig. 8**d), most samples are distributed on both sides of dissolution line, indicating gypsum dissolution is limited (Eq. 16). This is consistent with the undersaturation of gypsum observed in the water samples (Fig. S3). **Fig. 8**e shows the correlation between (Ca^{2+}+Mg^{2+}) and SO_4^{2-}after subtracting the Ca^{2+} and Mg^{2+} contained in carbonate rocks. Some samples in Group 2 exhibit excess SO_4^{2-}. This may arise from the oxidation of pyrite within the strata or the oxidative hydrolysis of H_2S and SO_2 transported from deep into geothermal reservoirs. A good linear correlation between Fe and SO_4^{2-} in the Group 2 geothermal water suggests a contribution from pyrite dissolution (Fig. S2). Similarly, it is observed that the higher scores for PC2 (median = 0.88) and PC3 (median = 0.47) in the Group 2 (**Fig. 6**b**)** indicate that the dissolution of carbonate and sulfate minerals plays a dominant role, consistent with the prevalence of Ca-HCO_3 and Ca-SO_4 hydrochemical types. Group 3 shows unremarkable scores across the three factors, and it displays a hydrochemical shift from Na-HCO_3 to Ca-HCO_3, suggesting that the deep geothermal water may have experience significant mixing with shallow cold water as it rise toward the surface.

In summary, water-rock interactions are the primary factor controlling the chemical composition of thermal springs in the EHS, with the relative contributions of silicate, carbonate, and sulfate/sulfide dissolution being 33.9%, 27%, and 21.1%, respectively, following by deep fluid mixing (18.1%).

$$2NaAlSi_3O_8 + 3H_2O + CO_2 \rightarrow Al_2(Si2O_5)\,(OH)_4 + 4SiO_2 + 2Na^+ + 2HCO_3^- \quad (9)$$

$$2KAlSi_3O_8 + 3H_2O + CO_2 \rightarrow Al_2(Si2O_5)\,(OH)_4 + 4SiO_2 + 2K^+ + 2HCO_3^- \quad (10)$$

$$Ca^{2+} + 2NaX \rightarrow 2Na^+ + CaX_2 \quad (11)$$

$$CAI\text{-}I = (Cl^- - (Na^+ + K^+)) / Cl^- \quad (12)$$

$$CAI\text{-}II = (Cl^- - (Na^+ + K^+)) / (HCO_3^- + CO_3^{2-} + SO_4^{2-} + NO_3^-) \quad (13)$$

$$CaCO_3 + CO_2 + H_2O \rightarrow Ca^{2+} + 2HCO_3^- \quad (14)$$

$$CaMg(CO_3)_2 + 2CO_2 + 2H_2O \rightarrow Ca^{2+} + Mg^{2+} + 4HCO_3^- \quad (15)$$

$$CaSO_4 \cdot 2H_2O \rightarrow Ca^{2+} + SO_4^{2-} + 2H_2O \quad (16)$$

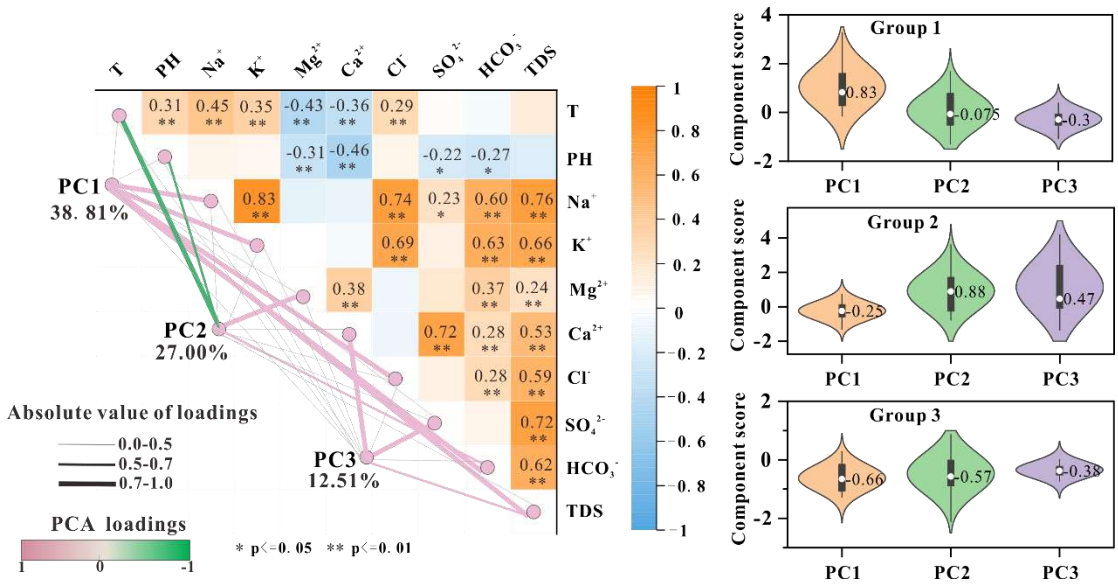


Fig. 6. (a) The results of Pearson correlation and PCA. (b) Violin plots of the factor scores of three groups of water samples.

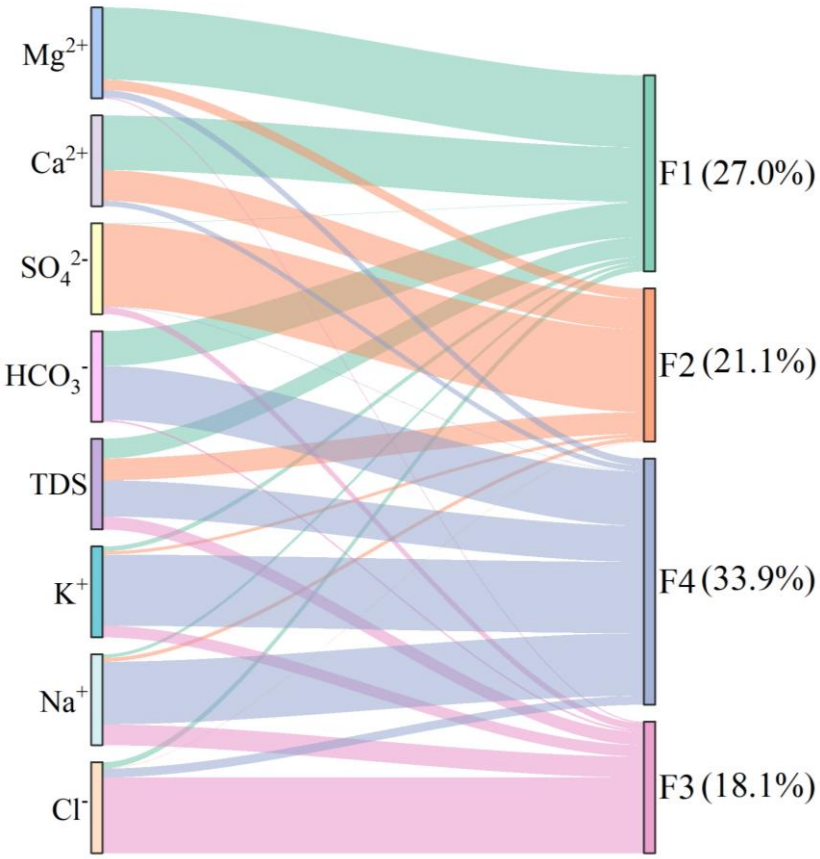


Fig. 7. The results of source apportionment based on the PMF model.

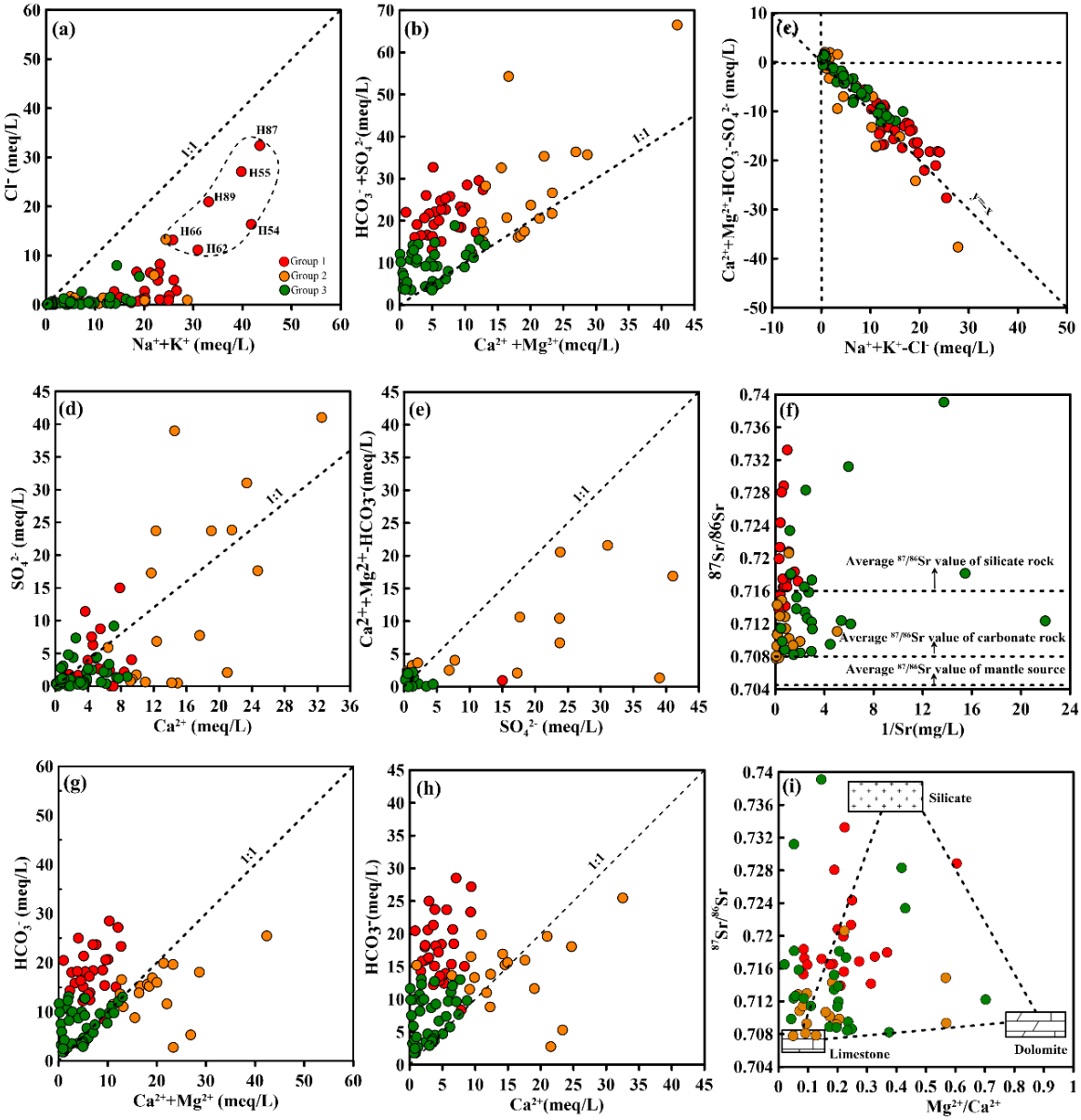


Fig. 8. Diagram of ion ratios in geothermal water: (a) ($Na^+ + K^+$) vs. Cl^-; (b) ($Ca^{2+} + Mg^{2+}$) vs. ($HCO_3^- + SO_4^{2-}$); (c) ($Na^+ + K^+ - Cl^-$) vs. ($Ca^{2+} + Mg^{2+} - SO_4^{2-} - HCO_3^-$); (d) Ca^{2+} vs. SO_4^{2-};(e) SO_4^{2-} vs. ($Ca^{2+} + Mg^{2+} - HCO_3^-$); (f) $^{87}Sr/^{86}Sr$ vs.1/Sr; (g) HCO_3^- vs. ($Ca^{2+} + Mg^{2+}$); (h) HCO_3^- vs. Ca^{2+}; (i) $^{87}Sr/^{86}Sr$ vs. ($Mg^{2+} + Ca^{2+}$)

5.2 Arsenic and fluorine sources analysis

Arsenic and fluorine tend to be enriched in the geothermal systems, and may pose potential risks to both groundwater and surface water environments. According to the World Health Organization (WHO) Guidelines for Drinking-water Quality, the permissible levels for As and F are 10 μg/L and 1.5 mg/L, respectively (WHO 2017). In this study, arsenic concentrations exceeding 10 μg/L were detected in 55% of the samples, and fluoride concentrations exceeding 1.5 mg/L were found in 76% of the samples. Among these, the concentrations of As in some samples from the group 1 approached 2,000 μg/L, while the concentrations of F in samples from the group 3 approached 20 mg/L, far exceeding the limits set by the WHO.

There are significant differences in the As concentrations among the three groups in the EHS, with the mean values ranked as follows: Group 1 > Group 2 > Group 3 (**Fig. 4**). Current research generally indicates that arsenic in geothermal water primarily originates from leaching of reservoir rocks or the input of deep hydrothermal fluids (Baba et al. 2021; Morales-Simfors and Bundschuh 2022). As mentioned previously, the chemical composition of the geothermal water in the EHS is significantly controlled by the dissolution of silicate minerals. Arsenic displays positive associations with both Na^+ and K^+ in the Group1 and Group3 (Fig. S5), indicating that the leaching of silicate rocks in deep geothermal reservoirs is a major contributor to the arsenic in geothermal water (Zhuang et al. 2025). Furthermore, B and Li are signature elements of deep hydrothermal fluids in geothermal systems and can serve as indicators of deep fluid sources (Li et al. 2022; Zhang et al. 2025). As exhibits significant positive correlations with Cl^-, B, and Li in Group 1 (Fig. S5b), demonstrating a pattern of synchronous high enrichment. This indicates that the high concentration of arsenic is likely influenced by the input of deep fluids (Guo et al. 2019). Therefore, the enrichment of arsenic in the Group 1 result from the combined effects of the leaching of reservoir rocks and the input of deep fluids.

Arsenic-bearing sulfide minerals, such as arsenopyrite, are commonly found in granite, volcanic rock, and metamorphic rock (Ballantyne and Moore 1988; Smedley and Kinniburgh 2002). The geothermal springs in Group 2 are characterized by high Ca^{2+}, high SO_4^{2-}, and weak acidity. In this group, the correlation between As and Cl^- is weak (Fig. S5c), indicating that its source mechanism differs from that of Group 1. As shows a positive correlation trend with SO_4^{2-} and is significantly positively correlated with T (Fig. S5c), hinting that the oxidation and dissolution of arsenic-bearing sulfide minerals driven by high temperatures may be the source of arsenic in Group 2.

The distribution of F^- in geothermal waters across the three groups in the EHS differed from that of As. Specifically, the concentrations of F in Groups 1 and 3 were similar (mean: 4-5 mg/L), significantly higher than those in Group 2 (mean: 2 mg/L) (**Fig. 3**). Fluorine is typically enriched in acidic rocks, particularly in areas with granite and metamorphic rocks (Chowdhury et al. 2019). Experiments indicate that the rapid dissolution of granite and biotite can elevate fluoride concentrations in water to 6 mg/L (Chae et al. 2006). Accordingly, the high concentration of F^- in thermal springs is closely related to the widely exposed Himalayan granite in the EHS. As geothermal fluids circulate deeply along fault zones, they strongly leach these fluorine-bearing minerals under high-temperature conditions, which promotes the continuous release of F into the liquid phase (Huang et al. 2025). As revealed by the correlation analysis, F^- and T show a robust positive relationship (Fig. S5a). This further indicates that temperature is a key factor controlling the dissolution of fluorine-bearing minerals and driving the enrichment of F^-.

Fluorite (CaF_2) dissolution is the common mechanism for F^- enrichment in geothermal

systems (Nordstrom 2022). In this study, a significant negative correlation between F^- and Ca^{2+} is observed in samples from Group 1 and Group 3 (Fig. S5a, d). This indicates a geochemical process involving the fluorite dissolution and calcite precipitation occur together (Eq.17, 18) (Liu et al. 2024a). The dissolution of fluorite continuously releases Ca^{2+} and F^- into the geothermal waters. Meanwhile, the high HCO_3^- concentration provides an abundant source of carbonate for calcite precipitation. This causes Ca^{2+} to be continuously removed from the liquid phase. Meanwhile, Na^+/Ca^{2+} cation exchange further consumes Ca^{2+} in the water, keeping the solution undersaturated with respect to fluorite (Wang et al. 2021). As a result, the fluorite dissolution reaction proceeds continuously in a positive direction, promoting the continuous enrichment of F^-. Calculations of saturation indices show that most samples exhibit supersaturation with respect to calcite but undersaturated towards fluorite (Fig. S3), consistent with the aforementioned mechanism.

$$CaF_2 \rightarrow Ca^{2+} + 2F^- \quad (17)$$

$$CaF_2 + HCO_3^- \rightarrow CaCO_3 + 2F^- + H^+ \quad (18)$$

5.3 Isotopic Characteristics of thermal spring

Strontium isotopes serve as robust tracers for identifying water-rock interaction processes (Guo et al. 2010; Stettler 1977). Generally, carbonate rocks are enriched in strontium but exhibit low $^{87}Sr/^{86}Sr$ ratios, whereas silicate rocks have low strontium concentrations but high $^{87}Sr/^{86}Sr$ ratios (Palmer and Edmond 1992). The average $^{87}Sr/^{86}Sr$ ratio for marine carbonate rocks is 0.708 (Veizer and Compston 1974), the average $^{87}Sr/^{86}Sr$ ratio for continental silicate rocks is 0.716 (Taylor and McLennan 1985), and the average $^{87}Sr/^{86}Sr$ ratio for mantle-derived materials is 0.704 (Hart 1984). As shown in **Fig. 8**f, the water samples in Group 2 near the average value of the carbonate rocks and display geochemical characteristics dominated by limestone dissolution (**Fig. 8**i), suggesting that geothermal water reservoir may be carbonate rock sequences. Most water samples in Group 1 are mainly distributed near the endmembers of silicate rocks (**Fig. 8**i, f), suggesting that their geothermal reservoirs consist of granite and metamorphic rocks. Group 3 samples are relatively dispersed, reflecting the mixed influence of carbonate and silicate dissolution, with some samples showing contributions from dolomite dissolution (**Fig. 8**i). Notably, $^{87}Sr/^{86}Sr$ of some samples in Groups 1 and 3 are significantly higher than the average value of silicate rocks (**Fig. 8**f). This feature is consistent with long-term water-rock interaction between geothermal water and the leucogranite exposed in the EHS. This leucogranite has a high Rb/Sr ratio, which is attributed to its source in ancient argillaceous metamorphic rocks that formed by partial melting and subsequently enriched radioactive strontium during its evolution (Liu et al. 2011).

$\delta^{18}O$ and δD are effective indicators for identifying the recharge sources of geothermal water and tracking geochemical evolution (Craig 1961). As shown in the **Fig. 9**, all the samples fall on or close to the GMWL and LMWL, indicating the meteoric precipitation is the main

recharge source. Simultaneously, enrichment of $\delta^{18}O$ is observed in a few samples, indicating significant rock-water interactions (**Fig. 9**a). In geothermal systems, water-rock interactions may lead to oxygen isotope exchange, specifically the transfer of ^{18}O from the ^{18}O-enriched reservoir rocks to the water, thereby increases the $\delta^{18}O$ value of the thermal water and forms a typical "oxygen drift" phenomenon (Yi et al. 2021).

Hydrothermal fluids can participate in geothermal circulation through fault fractures, enhancing the ^{18}O drift (Cao et al. 2025; Li et al. 2024). In the **Fig. 9**d, all the sample in the Group 2 close to the LMWL, indicating that they have not been significantly influenced by magmatic fluids. In contrast, several samples with high Cl^- in Group 1(e.g., H66, H67, H83) lie between the snowmelt and magmatic water end-members (**Fig. 9**b) and have high concentrations of B, and Li (**Fig. 2** and Table S1), implying contributions from deep fluids. Although some samples in Group 3 show a similar distribution trend (**Fig. 9**c), their Cl^-, B, and Li concentrations are significantly lower (**Fig. 2**.). This reflects relatively to deep fluid input, rock-water interaction is the dominant factor at high-temperature. The d-excess value is often used to indicate the intensity of water-rock interactions (Zhang et al. 2021). The d-excess values of samples in Group 1 are lower than those of Group 3 (Fig. S6), suggesting that the former has undergone more intense water-rock interaction, corresponding to higher reservoir temperatures, prolonged fluid residence, or a greater extent of water-rock exchange.

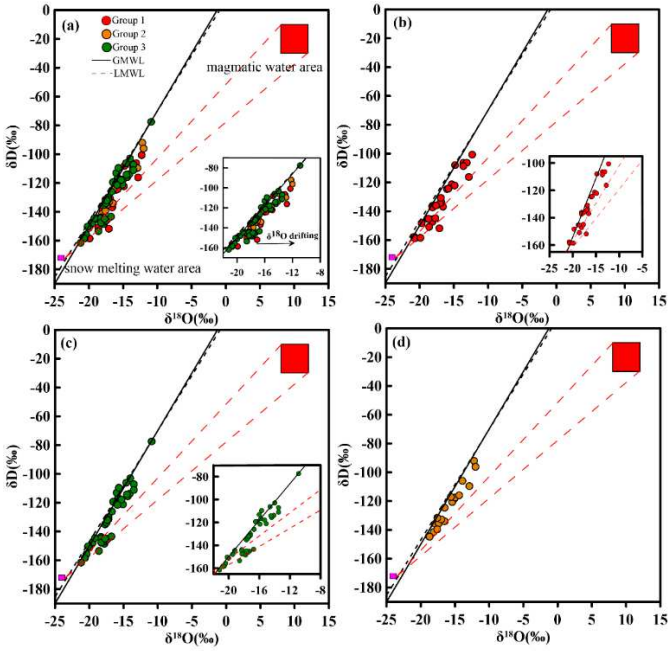


Fig. 9. Scatter plot of δD and $\delta^{18}O$ for all the geothermal samples in the EHS. Global Meteoric Water Line (GMWL): $\delta D = 8*\delta^{18}O + 10$ (Craig, 1961); Local Meteoric Water Line (LMWL): $\delta D = 7.67*\delta^{18}O + 6.7$ (Bershaw et al. 2012); The snowmelt water was cited from (Guo et al. 2014); the magmatic water area (δD: −20 ± 10 ‰; $\delta^{18}O$: +10 ± 2 ‰) was plotted from (Giggenbach 1992).

5.4 Geothermal reservoir temperature and circulation depth calculation

Reservoir temperature is one of the important parameters for assessing hydrothermal

resources. Researchers commonly apply solute geothermometers based on mineral-fluid equilibrium, such as cation geothermometers (e.g., Na-K, K-Mg) and the SiO_2 geothermometer (Arnorsson et al. 1983; Fournier 1977c; Giggenbach et al. 1983). However, the majority of these thermometers assume equilibrium with a single mineral phase, and the chemical composition of geothermal water can be altered during its ascent to the surface. As a result, the temperatures estimated by different geothermometers often show significant discrepancies. The Na-K-Mg triangular diagram can help evaluate the suitability of different cation geothermometers by assessing the water-rock equilibrium state (Giggenbach 1988). As shown in **Fig. 10**, the samples H24, H51, H67 in Group 1, and H5, H6, H31, H65 in Group 3 fall in the partially equilibrated region, with equilibrium temperatures ranging between 100-160°C and 200-240°C, respectively. But, all the water samples in Group 2 are concentrated in the lowermost right corner of the immature water region, indicating either mixing with a large amount of shallow cold water or insufficient water-rock interaction (Tian et al. 2019). Therefore, the reservoir temperatures estimated for the thermal waters using cation geothermometers are unreliable. Silica-based geothermometers, including quartz, chalcedony, and amorphous silica, derive reservoir temperature from silica concentrations. The SI values for chalcedony and quartz range from -2.5 to 0.7 and from -2.1 to 1.1, respectively. In the plot of log (K^2/Mg) versus log (SiO_2), almost all the samples are dispersed in the quartz and chalcedony lines, indicating that SiO_2 geothermometers may be more accurate (Erbaş and Bozdağ 2022). Using Equations (3)-(5), the calculated reservoir temperatures for the thermal waters range from 30°C to 197°C, 21°C to 215°C, and 4°C to 200°C, respectively. The SiO_2 geothermometer is applicable to thermal waters with temperatures between 20°C and 250°C (Dulanya et al. 2010). When the water temperature does not exceed 110°C, chalcedony is the key mineral controlling the silica concentration in water, whereas quartz becomes the dominant mineral when the temperature exceeds 120°C (Li et al., 2018a). According to this principle, the reservoir temperatures for Groups 1, 2, and 3, as calculated using a silica thermometer, are 49-138°C, 43-123°C, and 52-215°C, respectively.

However, geothermal water undergoes varying degrees of mixing with cold water as it migrates upward, and the quartz and chalcedony in some samples are in an unsaturated state. the results estimated using the silica geothermometer represent only the minimum temperature of the reservoir, and the impact of mixing on reservoir temperature estimates must be taken into account. Accordingly, we introduced the silica-enthalpy equation to retroactively calculate the SiO_2 concentration and temperature of deep geothermal water at equilibrium based on the SiO_2 concentration and the temperatures of both surface geothermal water and shallow cold water. Based on the results of the Eq. 6 and 7, the estimated reservoir temperatures for the Group1, Group2, and Group3 are 142 to 277°C, 156 to 233°C, and 125 to 269°C, respectively, with corresponding cold water mixing ratios of 47%-87%, 75%-91%, and 45%-91%, respectively

(Fig. 11). Although the reservoir temperatures of the three groups show no significant differences, the water samples in Group 2 have undergone more extensive mixing with cold water. The circulation depths for Group 1-3 geothermal water are 3832m to 7582m, 5485m to 6340m, and 3362m to 7354m, respectively based on the Eq.8.

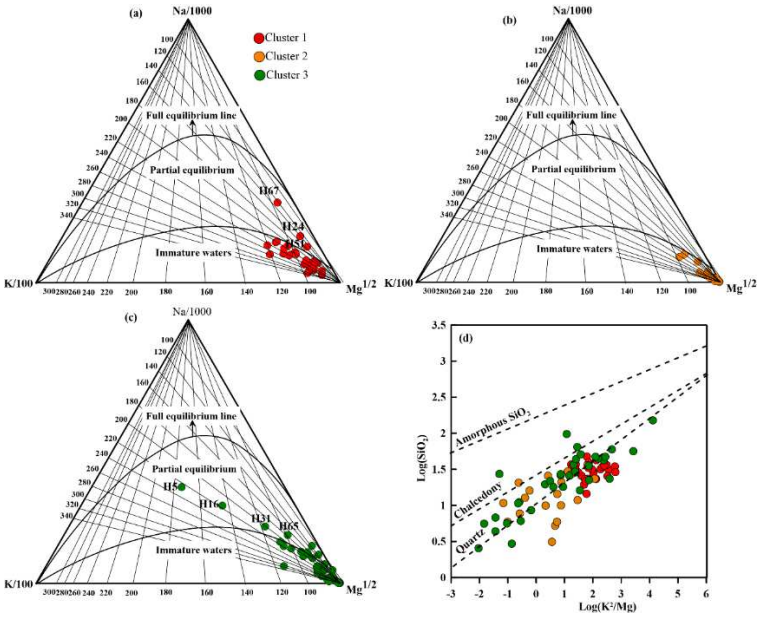


Fig. 10. (a, b, c) Na-K-Mg diagram for three groups of geothermal waters, (d) log (SiO_2) vs. log (K^2/Mg) binary diagram

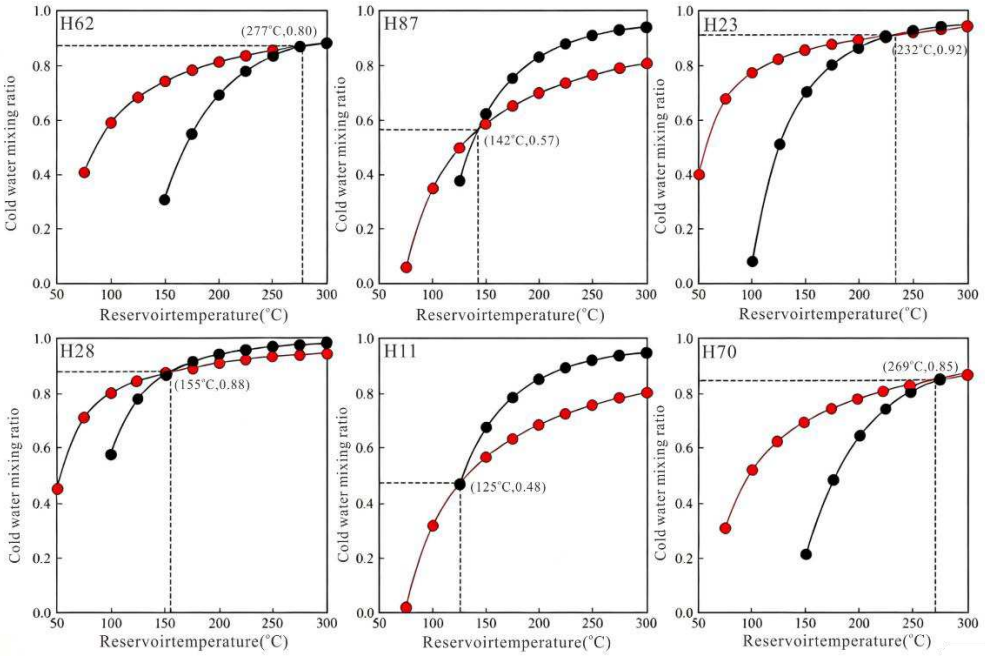


Fig. 11. Maximum and minimum reservoir temperatures estimated by the silica-enthalpy equation. H62 and H87 from Group1; H23 and H28 from Group2; H11 and H70 from Group3

5.5 Genesis model of geothermal water

Ongoing convergence between the Indo-Eurasian plates has driven rapid exhumation and erosion, which in turn triggered decompressional partial melting within the crust (Booth et al. 2009; Ding et al. 2001). This process has generated extensive melt bodies and pronounced heat flow

anomalies throughout the Tibetan Plateau (Jiang et al. 2019). It is generally acknowledged that the primary heat source for geothermal systems is the extensive partial melting layer found in the crust (Brown et al. 1996; Liao et al. 2026; Nelson et al. 1996). Previous geophysical data indicate that large low-velocity and high-conductivity zones are developed in the middle-lower crust of the Lhasa block and Qiangtang block in the EHS and its adjacent areas (Fig.S7), constituting the primary heat source for geothermal waters in this region (Liu et al. 2010; Peng et al. 2016; Yang et al. 2020). As shown in **Fig. 12**, isotopic analyses indicate that meteoric water constitutes the main recharge source for the thermal waters in the EHS. Meteoric water infiltrates downward along deep-seated faults, is heated by the partial melt bodies, and then ascends along water-conducting fault zones, forming a complete deep-circulation hydrothermal system. Due to differences in reservoir lithology and structure, the three groups of geothermal waters exhibit distinct hydrochemical characteristics. Group 1 geothermal water exhibits the greatest circulation depth (7582m), representing the "deep-circulation silicate" type. Fluids migrate along major faults cutting through granite and metamorphic basement, undergoing strong water–rock interaction with silicate minerals such as K-feldspar and albite under high-temperature conditions, continuously releasing Na^+, K^+, and HCO_3^-, while receiving inputs of deep-derived Cl^-, B, and Li. This results in high-salinity, high-As, high-B, and high-Li geothermal waters of Na-HCO_3 and Na-Cl types. The geothermal waters in Group 2 show no contribution from deep fluids. These fluids circulate primarily in Triassic carbonate reservoirs (with temperatures ranging from 156 °C to 233 °C), where the dissolution of calcite, dolomite, and gypsum dominates the hydrochemical evolution. In addition, the dissolution of pyrite in the strata is also a potential source for promoting SO_4^{2-} enrichment. During ascent, the geothermal fluids undergo substantial mixing with cold water (75%-91%), resulting in geothermal waters of predominantly HCO_3-Ca and SO_4-Ca (Mg) types. Group 3 represents the mixed type, in which both carbonate and silicate dissolution contribute to the hydrochemical composition, and the water types are predominantly Na–HCO_3 and Ca–HCO_3. The deep reservoir temperatures range from 125 °C to 269 °C. The dissolution of fluorine-bearing minerals in granite, promoted by high temperatures, results in exceptionally high F^- concentrations, which is the most distinctive feature of this group.

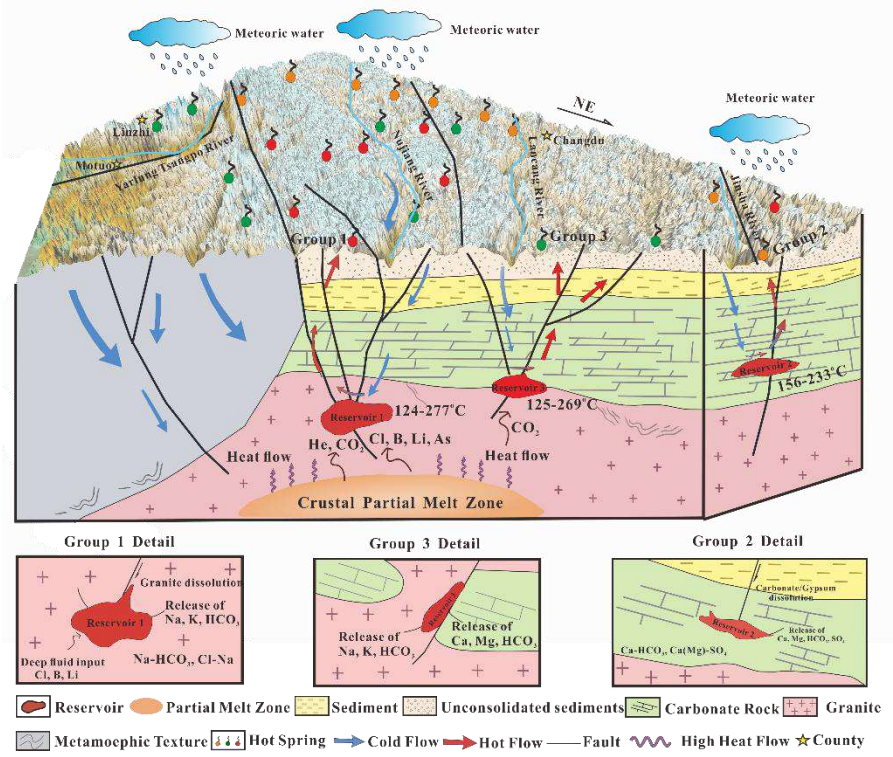


Fig. 12. Conceptual model of the geothermal water in the study area.

6. Conclusions

The present study used the SOM, multivariate statistics, and classic geochemical tools to investigative hydrochemistry, solute source, and water quality in thermal springs in the EHS. The several key findings are summarized as below:

(1) The three types of geothermal water are identified in the EHS based on the SOM. Group 1 is predominantly characterized by HCO_3-Na and Cl-Na, with significant enrichment of As, B, and Li, and is primarily controlled by the dissolution of silicate minerals and the input of deep fluids. Group 2 mainly exhibits HCO_3-Ca and SO_4-Ca, with solute components mainly comes from the dissolution of carbonate rocks and sulfate minerals. Group 3 belongs to the HCO_3-Ca·Na, characterized by a relatively high F^- content.

(2) The geothermal waters of Groups 1 to 3 are primarily recharged by atmospheric precipitation, while the contribution of magma water is limited. According to the silicon enthalpy equation, before mixing, the reservoir temperatures 142 to 277°C, 156 to 233°C, and 125 to 269°C, respectively, with corresponding cold water mixing ratios of 47%-87%, 75%-91%, and 45%-91%, respectively.

(3) The hydrochemical composition of thermal springs in the EHS is influenced by silicate weathering (33.9%), carbonate dissolution (27%), sulfate dissolution (21.1%), and deep fluid input (18.1%). The enrichment of As mainly originates from reservoir rock leaching and deep fluid contributions, whereas the enrichment of F is driven jointly by high-

temperature leaching and the process of fluorite dissolution coupled with calcite precipitation.

(4) The EWQI evaluation results indicate that the overall water quality of thermal spring is poor, with arsenic being the major controlling factor. The order of water quality from good to poor is Group 3 > Group 2 > Group 1.

CRediT authorship contribution statement

Bingyu Yao: Writing – original draft, Investigation, Formal analysis, Data curation. **Xiaocheng Zhou:** Writing – review & editing, Formal analysis, Funding acquisition. **Miao He:** Supervision, Investigation, Formal analysis, Data curation. **Zhaojun Zeng:** Investigation, Formal analysis,Visualization. **Yuwen Wang:** Methodology, Formal analysis, Software. **Jiao Tian:** Formal analysis, Data curation, Investigation. **Ruibing Li:**Visualization, Investigation, Data curation. **Han Yan:** Investigation, Data curation. **Yuxin Ren:** Investigation, Data curation. **Yinglin Han:** Methodology, Data curation. **Doudou Zha:** Investigation, Data curation.

Declaration of competing interest

The authors declare that they have no known competing financial interests or personal relationships that could have appeared to influence the work reported in this paper.

Acknowledgments

The work was funded by Deep Earth Probe and Mineral Resources Exploration - National Science and Technology Major Project (2024ZD1000500, 2025ZD1005100, 2025ZD1010303), Central Public-interest Scientific Institution Basal Research Fund (CEAIEF2025030101, CEAIEF20250601, CEAIEF2025080102), National Key Research and Development Project (2023YFC3012005-1), the National Natural Science Foundation of China (41673106), IGCP Project 724.

References

Abidi JH, Elzain HE, Sabarathinam C, Selmane T, Selvam S, Farhat B, Ben Mammou A, Senapathi V (2024) Evaluation of groundwater quality indices using multi-criteria decision-making techniques and a fuzzy logic model in an irrigated area. Groundw Sustain Dev 25:101122. https://doi.org/10.1016/j.gsd.2024.101122

Arnorsson S, Gunnlaugsson E, Svavarsson H (1983) The chemistry of geothermal waters in Iceland. III. Chemical geothermometry in geothermal investigations. Geochim Cosmochim Acta 47(3):567–577. https://doi.org/10.1016/0016-7037(83)90278-8

Baba A, Uzelli T, Sozbilir H (2021) Distribution of geothermal arsenic in relation to geothermal play types: a global review and case study from the Anatolian plate (Turkey). J Hazard Mater 414:125510. https://doi.org/10.1016/j.jhazmat.2021.125510

669 Ballantyne JM, Moore JN (1988) Arsenic geochemistry in geothermal systems. Geochim
670 Cosmochim Acta 52(2):475–483. https://doi.org/10.1016/0016-7037(88)90102-0
671 Battistel M, Hurwitz S, Evans WC, Barbieri M (2016) The chemistry and isotopic composition of
672 waters in the low-enthalpy geothermal system of Cimino-Vico Volcanic District, Italy. J
673 Volcanol Geoth Res 328:222–229. https://doi.org/10.1016/j.jvolgeores.2016.11.005
674 Bershaw J, Penny SM, Garzione CN (2012) Stable isotopes of modern water across the Himalaya
675 and eastern Tibetan Plateau: implications for estimates of paleoelevation and paleoclimate. J
676 Geophys Res Atmos 117. https://doi.org/10.1029/2011JD016132
677 Booth AL, Chamberlain CP, Kidd WSF, Zeitler PK (2009) Constraints on the metamorphic
678 evolution of the eastern Himalayan syntaxis from geochronologic and petrologic studies of
679 Namche Barwa. GSA Bull 121(3–4):385–407. https://doi.org/10.1130/B26041.1
680 Brown L, Zhao W, Nelson K, Hauck M, Alsdorf D, Ross A, Cogan M, Clark M, Liu X, Che J (1996)
681 Bright spots, structure, and magmatism in southern Tibet from INDEPTH seismic reflection
682 profiling. Science 274(5293):1688–1690. https://doi.org/10.1126/science.274.5293.1688
683 Burnside NM, Westaway R, Banks D, Zimmermann G, Hofmann H, Boyce AJ (2019) Rapid water-
684 rock interactions evidenced by hydrochemical evolution of flowback fluid during hydraulic
685 stimulation of a deep geothermal borehole in granodiorite: Pohang, Korea. Appl Geochem
686 111:104445. https://doi.org/10.1016/j.apgeochem.2019.104445
687 Cao R, Liu Q, Gao R, Dor J, Yan Y, Chen D, Poliakova M, Wan S (2025) Integrated mechanisms of
688 geothermal anomalies in the eastern Himalayan syntaxis: insights from crustal partial melting
689 and fault-controlled fluid circulation. J Hydrol Reg Stud 61:102726.
690 https://doi.org/10.1016/j.ejrh.2025.102726
691 Chae GT, Yun ST, Kwon MJ, Kim YS, Mayer B (2006) Batch dissolution of granite and biotite in
692 water: implication for fluorine geochemistry in groundwater. Geochem J 40(1):95－102.
693 https://doi.org/10.2343/geochemj.40.95
694 Chowdhury A, Adak MK, Mukherjee A, Dhak P, Khatun J, Dhak D (2019) A critical review on
695 geochemical and geological aspects of fluoride belts, fluorosis and natural materials and other
696 sources for alternatives to fluoride exposure. J Hydrol 574:333–359.
697 https://doi.org/10.1016/j.jhydrol.2019.04.033
698 Craig H (1961) Isotopic variations in meteoric waters. Science 133(3465):1702–1703.
699 https://doi.org/10.1126/science.133.3465.1702
700 Ding L, Zhong D, Yin A, Kapp P, Harrison TM (2001) Cenozoic structural and metamorphic
701 evolution of the eastern Himalayan syntaxis (Namche Barwa). Earth Planet Sci Lett
702 192(3):423–438. https://doi.org/10.1016/S0012-821X(01)00463-0
703 Dulanya Z, Morales-Simfors N, Sivertun Å (2010) Comparative study of the silica and cation

geothermometry of the Malawi hot springs: potential alternative energy source. J Afr Earth Sci 57(4):321–327. https://doi.org/10.1016/j.jafrearsci.2009.11.001

Erbaş HA, Bozdağ A (2022) Hydrogeochemical characteristics and evaluation of the geothermal fluids in the Gazlıgöl geothermal field (Afyonkarahisar), Western Anatolia, Turkey. Geothermics 105:102543. https://doi.org/10.1016/j.geothermics.2022.102543

Fournier RO, Truesdell AH (1974) Geochemical indicators of subsurface temperature. Part II. Estimation of temperature and fraction of hot water mixed with cold water. J Res US Geol Surv 2(3):263–270

Fournier R (1977a) Chemical geothermometers and mixing models for geothermal systems. Geothermics 5(1–4):41–50. https://doi.org/10.1016/0375-6505(77)90007-4

Fournier R (1977b) A review of chemical and isotopic geothermometers for geothermal systems. In: Proceeding of the Symposium on Geothermal Energy. Cento Scientific Program, pp. 133–143.

Fournier RO (1977c) Chemical geothermometers and mixing models for geothermal systems. Geothermics 5(1):41–50. https://doi.org/10.1016/0375-6505(77)90007-4

Giggenbach WF (1988) Geothermal solute equilibria. Derivation of Na-K-Mg-Ca geoindicators. Geochim Cosmochim Acta 52(12):2749–2765. https://doi.org/10.1016/0016-7037(88)90143-3

Giggenbach WF (1992) Isotopic shifts in waters from geothermal and volcanic systems along convergent plate boundaries and their origin. Earth Planet Sci Lett 113(4):495–510. https://doi.org/10.1016/0012-821X(92)90127-H

Giggenbach WF, Gonfiantini R, Jangi BL, Truesdell AH (1983) Isotopic and chemical composition of Parbati Valley geothermal discharges, North-West Himalaya, India. Geothermics 12(2):199–222. https://doi.org/10.1016/0375-6505(83)90030-5

Goswami S, Rai AK (2025) Assessment of hot-springs and geothermal prospects for sustainable energy goals. J Clean Prod 512:145637. https://doi.org/10.1016/j.jclepro.2025.145637.

Guo Q (2012) Hydrogeochemistry of high-temperature geothermal systems in China: a review. Appl Geochem 27(10):1887–1898. https://doi.org/10.1016/j.apgeochem.2012.07.006

Guo Q, Planer-Friedrich B, Liu M, Yan K, Wu G (2019) Magmatic fluid input explaining the geochemical anomaly of very high arsenic in some southern Tibetan geothermal waters. Chem Geol 513:32–43. https://doi.org/10.1016/j.chemgeo.2019.03.008

Guo Q, Wang Y, Liu W (2010) O, H, and Sr isotope evidences of mixing processes in two geothermal fluid reservoirs at Yangbajing, Tibet, China. Environ Earth Sci 59(7):1589–1597. https://doi.org/10.1007/s12665-009-0145-y

Guo QH, Liu ML, Li JX, Zhang XB, Wang YX (2014) Acid hot springs discharged from the Rehai

hydrothermal system of the Tengchong volcanic area (China): formed via magmatic fluid absorption or geothermal steam heating? Bull Volcanol 76(10):868. https://doi.org/10.1007/s00445-014-0868-9

Hart SR (1984) A large-scale isotope anomaly in the Southern Hemisphere mantle. Nature 309(5971):753–757. https://doi.org/10.1038/309753a0

Huang X, Huang J, Xie Y, Zhu B, Feng T, Wu H, Wang Y, Zhou P, Liu G, Wang Y, Zhang Y (2026) A comparative study of hydrochemical signatures and formation mechanisms of geothermal waters in the tensile and shear faults of the Tibetan Plateau. Geothermics 135:103540. https://doi.org/10.1016/j.geothermics.2025.103540

Huang X, Wang S, Wang S, Xiao Z, Zhang M, Zhang H, Qi S (2025) Fluoride in geothermal water: occurrence, origin, migration and environmental impact. J Geochem Explor 270:107640. https://doi.org/10.1016/j.gexplo.2024.107640

Jiang G, Hu S, Shi Y, Zhang C, Wang Z, Hu D (2019) Terrestrial heat flow of continental China: updated dataset and tectonic implications. Tectonophysics 753:36–48. https://doi.org/10.1016/j.tecto.2019.01.006

Jiménez J, Marazuela MÁ, Auqué LF, Baquedano C, Martínez-León J, Gasco-Cavero S, Santamarta JC, García-Gil A (2026) Multicomponent solute geothermometry coupled with geochemical modeling of secondary processes in thermal waters from volcanic islands as a versatile tool for geothermal exploration. Insights from La Palma (Canary Islands). Geothermics 136:103583. https://doi.org/10.1016/j.geothermics.2025.103583

Kobare ND, Kashiwaya K, Koike K, Mahecha A (2025) Circulation process of geothermal fluids and potential assessment of geothermal resources in the Songwe half-graben and Kiejo-Mbaka prospects in southwestern Tanzania: insight from hydrochemistry and stable isotopes. Geothermics 130:103347. https://doi.org/10.1016/j.geothermics.2025.103347

Kohonen T (1982) Self-organized formation of topologically correct feature maps. Biol Cybern 43(1):59–69. https://doi.org/10.1007/BF00337288

Li J, Sagoe G, Yang G, Lu G (2018a) Evaluation of mineral-aqueous chemical equilibria of felsic reservoirs with low-medium temperature: a comparative study in Yangbajing geothermal field and Guangdong geothermal fields. J Volcanol Geotherm Res 352:92–105. https://doi.org/10.1016/j.jvolgeores.2018.01.008

Li J, Wang X, Ruan C, Sagoe G, Li J (2022) Enrichment mechanisms of lithium for the geothermal springs in the southern Tibet, China. J Hydrol 612:128022. https://doi.org/10.1016/j.jhydrol.2022.128022.

Li J, Yang G, Sagoe G, Li Y (2018b) Major hydrogeochemical processes controlling the composition of geothermal waters in the Kangding geothermal field, western Sichuan Province. Geothermics 75:154–163. https://doi.org/10.1016/j.geothermics.2018.04.008

Li M, Zhang G, Zhang X, Chen X, Zheng C, Yang H, Li Q, Fan Q (2025) Hydrogeochemical coupling evolution of surface water and groundwater in the alpine watershed and salinity enrichment mechanism in the salt marsh plain on the Tibetan Plateau. J Hydrol 662:134029. https://doi.org/10.1016/j.jhydrol.2025.134029

Li X, Qi J, Yi L, Xu M, Zhang X, Zhang Q, Tang Y (2021) Hydrochemical characteristics and evolution of geothermal waters in the eastern Himalayan syntaxis geothermal field, southern Tibet. Geothermics 97:102233. https://doi.org/10.1016/j.geothermics.2021.102233

Li Y, Zhou X, Huang T, Tian J, He M, Zhu X, Li J, Zhang Y, Wu Z, Li B, Yan Y, Wang Y, Yao B, Zeng Z, Xing G, Cui S (2024) Origins of volatiles and helium fluxes from hydrothermal systems in the Eastern Himalayan Syntaxis and constraints on regional heat and tectonic activities. J Hydrol 631:130776. https://doi.org/10.1016/j.jhydrol.2024.130776

Liao M, Cheng Y, Han B, Pang Z (2026) Control of crustal melt migration on geothermal system development in the Daggyai area, southern Tibet: insights from 3D magnetotelluric imaging. Tectonophysics 919:231032. https://doi.org/10.1016/j.tecto.2025.231032

Liao X, Jiang H, Xu Z, Xiao Y, Song Z, Ouyang J, Zhang Y, Wu X (2020) Hydrogeochemical characteristics and genesis mechanism of geothermal water in Awang, Eastern Tibet. J Eng Geol 28(4):916–924. https://doi.org/10.13544/j.cnki.jeg.2019-573 (in Chinese with English abstract).

Liu C, Diao Z, Zhang Z (1996) Tethyan Geology of Western Sichuan and Eastern Tibet. Southwest Jiaotong University Press, Chengdu.

Liu J, Ren Z, Yu Q, Qi K, Wu H, Wang Z, Zhang G, Zhang Y, Jia M, Jia P (2024a) Hydrochemical processes and fluoride enrichment patterns in high-fluoride geothermal water in the Weihe Basin, China. J Hazard Mater 480:136468. https://doi.org/10.1016/j.jhazmat.2024.136468

Liu M, Bai D, Xiao P (2010) The electrical conductivity structure of the eastern Tibetan Plateau and its tectonic implications. Seismol Geol 32(1):51–58 (in Chinese with English abstract).

Liu Y, Siebel W, Theye T, Massonne H-J (2011) Isotopic and structural constraints on the late Miocene to Pliocene evolution of the Namche Barwa area, eastern Himalayan syntaxis, SE Tibet. Gondwana Res 19(4):894–909. https://doi.org/10.1016/j.gr.2010.11.005

Liu Z, Wang X, Wan X, Jia S, Mao B (2024b) Evolution origin analysis and health risk assessment of groundwater environment in a typical mining area: insights from water-rock interaction and anthropogenic activities. Environ Res 252:118792. https://doi.org/10.1016/j.envres.2024.118792

Lu R, Xie W, Liu B, Zhang S, Zhu J, Lin W (2024) Geothermal fluid chemistry and isotope for interpreting the formation of complex geothermal system in the Gonghe Basin, northeastern Tibetan Plateau. J Hydrol 633:130813. https://doi.org/10.1016/j.jhydrol.2024.130813

Luo H, Yuan X, Zhao X, Wang Y, Wu H, Zhou P, Zhang H, Liu G, Zhang Y (2025) A conceptual model and changing trends for the Yangbajing geothermal field in the Tibetan Plateau: new

insights from hydrochemistry and multi-isotopes. Geothermics 131:103391. https://doi.org/10.1016/j.geothermics.2025.103391

McCleskey RB, Roth DA, Mahony D, Nordstrom DK, Kinsey S (2019) Sources, fate, and flux of geothermal solutes in the Yellowstone and Gardner Rivers, Yellowstone National Park, WY. Appl Geochem 111:104458. https://doi.org/10.1016/j.apgeochem.2019.104458

Mia MY, Haque ME, Islam ARMT, Jannat JN, Jion MMMF, Islam MS, Siddique MAB, Idris AM, Senapathi V, Talukdar S, Rahman A (2023) Analysis of self-organizing maps and explainable artificial intelligence to identify hydrochemical factors that drive drinking water quality in Haor region. Sci Total Environ 904:166927. https://doi.org/10.1016/j.scitotenv.2023.166927

Mjami NB, Kimambo C, Ayeng'o S, Orozova-Bekkevold I (2025) Prospects and challenges for utilisation of low- to medium-temperature geothermal resources in Tanzania. Geothermics 129:103288. https://doi.org/10.1016/j.geothermics.2025.103288

Morales-Simfors N, Bundschuh J (2022) Arsenic-rich geothermal fluids as environmentally hazardous materials-a global assessment. Sci Total Environ 817:152669. https://doi.org/10.1016/j.scitotenv.2021.152669

Naseer MT (2026) Spectral decomposition-based temperature and water saturation-constrained dynamical simulations detect high-temperature geothermal energy resource. Renew Energy 256:123356. https://doi.org/10.1016/j.renene.2025.123356

Nelson KD, Zhao W, Brown L, Kuo J, Che J, Liu X, Klemperer S, Makovsky Y, Meissner R, Mechie J (1996) Partially molten middle crust beneath southern Tibet: synthesis of project INDEPTH results. Science 274(5293):1684–1688. https://doi.org/10.1126/science.274.5293.1684

Nordstrom DK (2022) Fluoride in thermal and non-thermal groundwater: insights from geochemical modeling. Sci Total Environ 824:153606. https://doi.org/10.1016/j.scitotenv.2022.153606

Palmer MR, Edmond JM (1992) Controls over the strontium isotope composition of river water. Geochim Cosmochim Acta 56(5):2099–2111. https://doi.org/10.1016/0016-7037(92)90332-D

Pan S, Kong Y, Wang K, Ren Y, Pang Z, Zhang C, Wen D, Zhang L, Feng Q, Zhu G, Wang J (2021) Magmatic origin of geothermal fluids constrained by geochemical evidence: implications for the heat source in the northeastern Tibetan Plateau. J Hydrol 603:126985. https://doi.org/10.1016/j.jhydrol.2021.126985

Pang Z, Kong Y, Li J, Tian J (2017) An isotopic geoindicator in the hydrological cycle. Procedia Earth Planet Sci 17:534–537. https://doi.org/10.1016/j.proeps.2016.12.135

Peng M, Jiang M, Li ZH, Xu Z, Zhu L, Chan W, Chen Y, Wang Y, Yu C, Lei J, Zhang L, Li Q, Xu L (2016) Complex Indian subduction style with slab fragmentation beneath the Eastern Himalayan Syntaxis revealed by teleseismic P-wave tomography. Tectonophysics 667:77–86. https://doi.org/10.1016/j.tecto.2015.11.012

Rahman ATMS, Kono Y, Hosono T (2022) Self-organizing map improves understanding on the

hydrochemical processes in aquifer systems. Sci Total Environ 846:157281. https://doi.org/10.1016/j.scitotenv.2022.157281

Robidoux P, Tardani D, Sánchez-Alfaro P, Liuzzo M, Morata D, Moussallam Y, Rose-Koga EF, Tassi F, Pérez-Flores P, Grassa F, Francofonte V (2025) Relationship of magmatic fluids to high-enthalpy geothermal systems: new insights from the Tolhuaca Geothermal System (TGS), Southern Andes. Chem Geol 681:122583. https://doi.org/10.1016/j.chemgeo.2024.122583

Schmidt G, Najem SA, Isenbeck-Schröter M, Freundt F, Kraml M, Aeschbach W (2017) $^{87}Sr/^{86}Sr$ ratios in thermal water from the southern Upper Rhine Graben, Germany. Procedia Earth Planet Sci 17:364–367. https://doi.org/10.1016/j.proeps.2016.12.092

Smedley PL, Kinniburgh DG (2002) A review of the source, behaviour and distribution of arsenic in natural waters. Appl Geochem 17(5):517–568. https://doi.org/10.1016/S0883-2927(02)00018-5

Song J (2010) Study on current movement characteristics and numerical simulation of the main faults around the Eastern Himalayan Syntaxis. Institute of Geology, China Earthquake Administration, Beijing, China.

Stettler A (1977) 87Rb-87Sr systematics of a geothermal water-rock association in the Massif Central, France. Earth Planet Sci Lett 34(3):432–438. https://doi.org/10.1016/0012-821X(77)90054-1

Tang FT, Song J, Cao ZQ, Deng ZH, Wang M, Xiao GR, Chen WT (2010) The movement characters of main faults around Eastern Himalayan Syntaxis revealed by the latest GPS data. Chin J Geophys 53:2119–2128. https://doi.org/10.3969/j.issn.0001-5733.2010.09.012

Tapponnier P, Xu Z, Roger F, Meyer B, Arnaud N, Wittlinger G, Yang J (2001) Oblique stepwise rise and growth of the Tibet Plateau. Science 294(5547):1671–1677. https://doi.org/10.1126/science.105978

Tian J, Pang Z, Wang Y, Guo Q (2019) Fluid geochemistry of the Cuopu high temperature geothermal system in the eastern Himalayan syntaxis with implication on its genesis. Appl Geochem 110:104422. https://doi.org/10.1016/j.apgeochem.2019.104422

Veizer J, Compston W (1974) 87Sr/86Sr composition of seawater during the Phanerozoic. Geochim Cosmochim Acta 38(9):1461–1484. https://doi.org/10.1016/0016-7037(74)90099-4

Wang Y, Li L, Wen H, Hao Y (2022) Geochemical evidence for the nonexistence of supercritical geothermal fluids at the Yangbajing geothermal field, southern Tibet. J Hydrol 604:127243. https://doi.org/10.1016/j.jhydrol.2021.127243

Wang Z, Guo H, Xing S, Liu H (2021) Hydrogeochemical and geothermal controls on the formation of high fluoride groundwater. J Hydrol 598:126372. https://doi.org/10.1016/j.jhydrol.2021.126372

World Health Organization (2026) Guidelines for Drinking-Water Quality: Fourth Edition

Incorporating the First, Second and Third Addenda. World Health Organization, Geneva. https://doi.org/10.9789240121225

Wostbrock JAG, Sharp ZD, Sanchez-Yanez C, Reich M, van den Heuvel DB, Benning LG (2018) Calibration and application of silica-water triple oxygen isotope thermometry to geothermal systems in Iceland and Chile. Geochim Cosmochim Acta 234:84–97. https://doi.org/10.1016/j.gca.2018.05.007

Xu Z, Ji S, Cai Z, Zeng L, Geng Q, Cao H (2012) Kinematics and dynamics of the Namche Barwa Syntaxis, eastern Himalaya: constraints from deformation, fabrics and geochronology. Gondwana Res 21(1):19–36. https://doi.org/10.1016/j.gr.2011.06.010

Xu ZQ, Li HB, Yang JS (2006) An orogenic plateau—the orogenic collage and orogenic types of the Qinghai-Tibet Plateau. Earth Sci Front 13(4):5–21 (in Chinese with English abstract)

Xu ZQ, Wang Q, Li ZH, Li HQ, Cai ZH, Liang FH, Dong HW, Cao H, Chen XJ, Huang XM, Wu C, Xu CP (2016) Indo-Asian collision: tectonic transition from compression to strike slip. Acta Geol Sin 90(1):1−23. https://doi.org/10.3969/j.issn.0001-5717.2016.01.001

Yang H, Xiao Y, Zhang Y, Wang L, Wang J, Hu W, Liu G, Liu F, Hao Q, Wang C, Xu X (2024) Lithology controls on the mixing behavior and discharge regime of thermal groundwater in the Bogexi geothermal field on Tibetan Plateau. J Hydrol 628:130523. https://doi.org/10.1016/j.jhydrol.2023.130523

Yang W, Jin S, Zhang L, Qu C, Hu X, Wei W, Yu C, Yu P (2020) The three-dimensional resistivity structures of the lithosphere beneath the Qinghai-Tibet Plateau. Chin J Geophys 63(3):817–827 (in Chinese with English abstract)

Yi L, Qi J, Li X, Xu M, Zhang X, Zhang Q, Tang Y (2021) Geochemical characteristics and genesis of the high-temperature geothermal systems in the north section of the Sanjiang Orogenic belt in southeast Tibetan Plateau. J Volcanol Geotherm Res 414:107244. https://doi.org/10.1016/j.jvolgeores.2021.107244

Yuan X, Zhang Y, Huang J, Pang Z, Huang H, Wang W, Wang Y, Chang M, Taussi M, Wang L (2025) Hydrochemistry and multi-isotopes for interpreting formation mechanisms of different-type geothermal waters in the Cuona-Woka Rift, southern Tibetan Plateau. Geosci Front 16(6):102170. https://doi.org/10.1016/j.gsf.2025.102170

Zhang C, Li X, Ma J, Fu C, Bai Z, Yu Q (2023) Characteristics and potential evaluation of geothermal resources in the eastern Himalayan syntaxis. Acta Geol Sin 97(8):2728–2741. https://doi.org/10.19762/j.cnki.dizhixuebao.2022089

Zhang F, Huang T, Man W, Hu H, Long Y, Li Z, Pang Z (2021) Contribution of recycled moisture to precipitation: a modified d-excess-based model. Geophys Res Lett 48(21):e2021GL095909. https://doi.org/10.1029/2021GL095909

Zhang Y, Huang J, Li X, Santosh M, Wang Y, Yuan X, Wang Y, Guo H, Zhao X, Huang X (2026)

Geothermal resources pathways: the hydrochemical evolution and genesis of geothermal waters in the Xianshuihe fault zone, eastern Qinghai-Xizang Plateau. Geothermics 136:103551. https://doi.org/10.1016/j.geothermics.2025.103551

Zhang Y, Tan H, Shi Z, Xue F, Zhang X, Ma H (2025) Decoding cycling and enrichment of boron and associated lithium in waters of the Tibetan Plateau with boron isotopes. Gondwana Res 141:120–134. https://doi.org/10.1016/j.gr.2025.02.006

Zhou H, Kuang X, Hao Y, Wang C, Feng Y, Zou Y, Zhu M, Zheng C (2023) Magmatic fluid input controlling the geochemical and isotopic characteristics of geothermal waters along the Yadong-Gulu rift, southern Tibetan Plateau. J Hydrol 619:129196. https://doi.org/10.1016/j.jhydrol.2023.129196

Zhu T, Wu Q, Gao S, Zeng J, Linghu K, Zhang X (2025) Comparative assessment of health risks and water quality of groundwater in urban and rural Guiyang, Southwest China: insights from PMF and Monte Carlo simulation. Ecotoxicol Environ Saf 299:118359. https://doi.org/10.1016/j.ecoenv.2025.118359

Zhuang S, Wang G, Zhou X, Shi Z, Yuan D, Tian J, He M, Zeng Z, Yan Y, Yao B, Wang Y, Xing G, Cui S (2025) Deciphering the distribution and enrichment of arsenic in geothermal water in the Red River Fault Zone, southwest China. J Hazard Mater 485:136756. https://doi.org/10.1016/j.jhazmat.2024.136756

Supplementary Files

This is a list of supplementary files associated with this preprint. Click to download.

- SupplementaryMaterials.zip